sustainability

MDPI

Article

Voltage Risk Zoning and Multi-Resource Coordinated Optimization for Active Distribution Networks Under Feeder Disconnection Faults

Jiangping Jing [1], Gaige Liang [2], Fei Xu [3,4], Ye Guo [1] and Ling Hao [3,4,*]

[1] State Grid Jiangsu Electric Power Co., Ltd., Nanjing 210000, China
[2] Xuzhou Power Supply Branch of State Grid Jiangsu Electric Power Co., Ltd., Xuzhou 221000, China
[3] Department of Electrical Engineering and Applied Electronic Technology, Tsinghua University, Beijing 100084, China
[4] State Key Laboratory of Operation and Control of New Power Systems, Tsinghua University, Beijing 100084, China
* Correspondence: haolg@foxmail.com

Abstract

Sustainable electricity systems require reliable power supply and the effective integration of distributed renewable energy. In active distribution networks, feeder disconnection can threaten both objectives by causing undervoltage during load transfer and creating overvoltage or reverse power flow risks under high photovoltaic (PV) generation. This paper proposes a post-fault coordination method integrating voltage risk zoning, resource direction screening, and restoration optimization. The method combines voltage and interface conditions, electrical distance changes, and resource sensitivities to identify and rank feasible regulation directions according to their benefits and costs. An outer procedure updates the risk zones and candidate set around a lexicographic mixed-integer linear optimization that prioritizes load restoration, constraint violation mitigation, and operating cost. Tests on a modified IEEE 33-bus system reduce candidate directions by 40% while preserving near-complete load restoration and modeled voltage and interface limit compliance, although operating cost, PV curtailment, and total computation time increase. A complementary study on the IEEE 123-node feeder with a fixed restored topology achieves the same percentage reduction in dispatch variables with essentially unchanged cost and a shorter dispatch solution time. The results inform sustainable distribution-network operation by quantifying trade-offs among service restoration, renewable-energy use, operating cost, and computational burden; screening benefits depend on the flexibility retained and the operating conditions.

Keywords: active distribution network; feeder disconnection; voltage risk zoning; undervoltage; restoration optimization

Check for updates

Academic Editors: Nadjet Zioui and Reda Dermouche

Received: 25 August 2026
Revised: 27 October 2026
Accepted: 29 October 2026
Published: 6 November 2026

Copyright: © 2026 by the authors. Licensee MDPI, Basel, Switzerland. This article is an open access article distributed under the terms and conditions of the Creative Commons Attribution (CC BY) license.

1. Introduction

The transition toward sustainable electricity systems requires reliable service and the effective integration of renewable generation. In active distribution networks, this requires coordinated source–grid–load–storage operation under bidirectional power flows and changing operating conditions. The integration of flexible resources, including distributed photovoltaic (PV) generation, distributed energy storage, soft open points (SOPs), static var generators (SVGs), and PV inverters, enhances the operational flexibility of distribution networks [1]. SOP-based voltage-support strategies can improve voltage stability in active

distribution networks [2]. Smart-PV voltage/VAR control further expands the available voltage-regulation capability [3]. These flexible resources provide an important technical basis for post-fault load restoration, voltage regulation, and operational risk mitigation. However, the increasing diversity of these resources also makes post-fault power-flow distributions, voltage characteristics, and regulation effects more complex.

This complexity is especially important after a feeder disconnection, when prolonged loss of supply can affect electricity-dependent activities and the reconfigured network may restrict renewable generation. Reliable restoration and the management of PV curtailment are therefore relevant, complementary operational dimensions of energy sustainability. Physics-informed distributed control can coordinate PV inverters without relying exclusively on a centralized voltage controller [4]. Accurate short-term PV forecasts can improve the temporal consistency of such decisions, although forecast uncertainty cannot be eliminated [5]. Regional autonomy and PV-storage coordination provide complementary voltage support when network operating conditions vary [6]. After a fault, however, the original supply path is interrupted, and the immediate task is to isolate the fault and restore de-energized loads without creating new voltage or loading violations; coordinated renewable resources can materially improve this restoration process [7].

Recent restoration research has therefore moved from static switching plans toward time-coupled coordination of topology and distributed resources. Konar et al. formulated autonomous restoration for DER-rich distribution systems as a distributed optimization problem [8]. Carrión et al. integrated Volt-Var devices, distributed energy resources, and energy storage into dynamic service restoration [9]. Repair scheduling, switching, and SOP operation have also been coordinated within a unified restoration framework [10]. For coupled energy systems, SOP-assisted reconfiguration can limit fault propagation and improve load-restoration capability [11]. Mobile energy storage introduces additional spatial flexibility when coordinated with distribution-network reconfiguration [12]. Comparative studies nevertheless show that the attainable restoration benefit depends on the SOP operating mode and its interaction with the post-fault topology [13].

A key unresolved issue is that post-fault voltage risk can develop in two opposite directions. Dispatchable-region analysis has shown that renewable accommodation depends jointly on network reconfiguration and the active- and reactive-power flexibility provided by SOPs [14]. Virtual power lines and SOPs can broaden the feasible operating region of AC/DC distribution systems, but the useful regulation direction remains state-dependent [15]. Sensitivity-based coordinated control can identify which resources are most effective for correcting a given voltage deviation [16]. For high-PV conditions, responsibility-driven mitigation methods have focused primarily on overvoltage caused by reverse power flow [17]. Topology changes further alter the mapping between control actions and bus voltages, motivating adaptive voltage-control policies [18]. Reactive-power control by PV inverters can mitigate voltage rise, but its effectiveness varies with feeder conditions and available inverter capacity [19].

The literature also indicates that voltage control, risk assessment, and restoration cannot be treated as independent tasks. Flexible interconnection can reduce losses and reverse-power-flow stress in high-PV distribution networks [20]. Risk-aware SOP allocation can limit voltage deviations under uncertain renewable output and load [21]. Coordinated planning of SOPs and energy storage can improve reliability under source-load imbalance [22]. During restoration, decentralized coordination can exploit SOP flexibility while reducing inter-system solution time [23]. Electrical-distance-based partitioning has been used to coordinate OLTCs, capacitor banks, and PV inverters under PV uncertainty [24]. Dynamic reconfiguration coordinated with mobile storage can simultaneously improve voltage quality and renewable-energy utilization [25]. Pattern-recognition-based reconfigu-

ration can identify topologies that alleviate steady-state voltage violations [26]. Explicitly modeling the switching sequence between feasible radial configurations can prevent impractical network transitions [27]. Combined central-local inverter control can provide system-wide coordination together with fast local voltage response [28].

Despite these advances, prior regional PV-storage coordination, sensitivity-based voltage control, and restoration optimization usually treat risk identification, regulation-direction selection, and topology/dispatch optimization as separate steps. The contribution here is their explicit coupling at the resource-direction level, together with a transparent separation between candidate scoring, top-K truncation, and outer state updates. The voltage-risk indices, sensitivity calculations, and DistFlow equations themselves are established tools; the revision therefore avoids presenting their integration as a new power-flow theory.

To address this need, this paper develops a risk-zoning and lexicographic restoration framework to assess operational trade-offs relevant to sustainable electricity supply. The main contributions are as follows:

(1) A risk-zoning and resource-direction screening approach is developed to distinguish high-voltage/reverse-flow and low-voltage/load-transfer risks, rank feasible regulation directions, and pass the selected union to a three-level MILP.
(2) The proposed framework establishes an auditable link between risk and control direction, while evaluating load restoration, voltage and interface compliance, PV curtailment, operating cost, and computational effort as distinct indicators.
(3) The screened feasible set is a subset of the all-resource set under matched constraints. Therefore, equal cost is possible when excluded directions are nonbinding, whereas a lower global optimum is not expected; any cost and total runtime penalties are reported rather than obscured.

The remainder of this paper is organized as follows. Section 2 presents voltage-risk identification and candidate resource-direction screening under feeder disconnection. Section 3 formulates the fault-reconfiguration and multi-resource coordination model. Section 4 reports the numerical results, including the IEEE 33-bus and IEEE 123-node studies. Section 5 discusses the operational implications and limitations, and Section 6 concludes the paper.

2. Voltage-Risk Identification and Regulation-Resource Screening Considering Feeder Disconnection Characteristics

2.1. Quantification of Feeder Disconnection Characteristics and Post-Fault Voltage-Risk Zoning

A feeder disconnection destroys the original supply path, while fault isolation and network reconfiguration alter power-flow distributions and resource voltage sensitivities. Two principal voltage risks may arise in an active distribution network. First, longer post-fault supply paths and increased transferred load can depress voltages at remote buses. Second, surplus PV power can flow backward through the reconfigured network, raising local voltages or increasing reverse power at the upstream-grid interface. Post-fault voltage-risk zones should therefore be identified rapidly to provide a physically relevant candidate set for subsequent multi-resource coordination.

To preserve a consistent comparison, zoning is evaluated on the reference post-fault state used to construct the candidate set. These two states are labelled separately throughout. The zoning rules apply only to energized buses; disconnected buses are recorded separately and are not treated as buffer buses.

Let $\boldsymbol{\Omega}_{\mathbf{N}}$, $\boldsymbol{\Omega}_{\mathbf{L}}$, $\boldsymbol{\Omega}_{\mathbf{F}}$, $\boldsymbol{\Omega}_{\mathbf{T}}$, and $\boldsymbol{\Omega}_{\mathbf{T}}^{\mathbf{F}}$ denote the sets of buses, branches, faulted branches, scheduling periods, and fault-duration periods, respectively. The operating state of branch (m,n) in period t is represented by $z_{mn,t}$, where $z_{mn,t} = 1$ if the branch is energized and

$z_{mn,t} = 0$ otherwise. To quantify the electrical coupling between a bus and the source, the electrical distance of bus i in period t is defined as

$$D_{i,t} = \sum_{(m,n)\in \boldsymbol{\Omega}_{i,t}^{\mathbf{path}}} \sqrt{r_{mn}^2 + x_{mn}^2} \tag{1}$$

where $\boldsymbol{\Omega}_{i,t}^{\mathbf{path}}$ is the set of branches on the supply path from the source bus to bus i under the current topology, and r_{mn} and x_{mn} are the resistance and reactance of branch (m,n), respectively.

To further describe how feeder disconnection and reconfiguration alter nodal supply paths, the fault-induced electrical-distance variation coefficient of bus i is defined as

$$k_{i,t}^{\mathrm{F}} = \frac{D_{i,t}^{\mathrm{F}} - D_i^0}{D_i^0} \tag{2}$$

where D_i^0 is the pre-fault electrical distance from the source to bus i, and $D_{i,t}^{\mathrm{F}}$ is the corresponding distance after fault isolation under the current topology in period t. Because reconfiguration changes the supply path, $D_{i,t}^{\mathrm{F}}$ is updated dynamically. A positive $k_{i,t}^{\mathrm{F}}$ indicates a longer post-fault path and greater undervoltage risk, whereas a negative value indicates a shorter path and relatively lower undervoltage risk.

In a distribution network with distributed PV, the imbalance between local PV generation and demand is a primary cause of reverse power flow and overvoltage. The net active-power injection at bus i in period t is

$$P_{i,t}^{\mathrm{net}} = P_{i,t}^{\mathrm{PV}} - P_{i,t}^{\mathrm{L}} \tag{3}$$

where $P_{i,t}^{\mathrm{PV}}$ and $P_{i,t}^{\mathrm{L}}$ are the active PV output and active load at bus i in period t, respectively. $P_{i,t}^{\mathrm{net}} > 0$ indicates a tendency for active power to be exported from the bus.

The surplus active PV power at bus i in period t is

$$P_{i,t}^{+} = \left[P_{i,t}^{\mathrm{net}}\right]^{+} = \max\left(0, P_{i,t}^{\mathrm{net}}\right) \tag{4}$$

where $[\cdot]+ = \max(0,\cdot)$.

The post-fault reverse-flow influence coefficient of bus i is then defined as

$$\chi_{i,t}^{\mathrm{rev}} = \alpha \frac{\sum\limits_{j\in\boldsymbol{\Omega}_{\mathrm{N}}} \overline{\mu}_j \left[S_{j,i,t}^{\mathrm{V,P,F}}\right]^{+}}{\max\limits_{h\in\boldsymbol{\Omega}_{\mathrm{N}}} \left(\sum\limits_{j\in\boldsymbol{\Omega}_{\mathrm{N}}} \overline{\mu}_j \left[S_{j,h,t}^{\mathrm{V,P,F}}\right]^{+}\right)} + (1-\alpha) \frac{\left[S_{0,i,t}^{\rho,\mathrm{P,F}}\right]^{+}}{\max\limits_{h\in\boldsymbol{\Omega}_{\mathrm{N}}} \left[S_{0,h,t}^{\rho,\mathrm{P,F}}\right]^{+}} \tag{5}$$

where $S_{j,i,t}^{\mathrm{V,P,F}}$ is the sensitivity of the voltage magnitude at bus j to active-power injection at bus i under the post-fault topology in period t; $S_{0,i,t}^{\rho,\mathrm{P,F}}$ is the sensitivity of the reverse loading ratio at the upstream-grid interface to active-power injection at bus i; $\overline{\mu}_j$ is the normalized nodal-importance weight and satisfies $\sum\limits_{j\in\boldsymbol{\Omega}_{\mathrm{N}}} \overline{\mu}_j = 1$; and $\alpha \in [0, 1]$ weights voltage-rise risk against interface reverse-loading risk [29]. Notably, the voltage and interface sensitivities are calculated by finite perturbations about the current reference state. Symmetric differences are used when both perturbation directions are feasible, and one-sided differences are used at device limits and at the zero-flow reverse-power kink. A denominator smaller than 10^{-9} is regularized, a bus without PV has zero surplus, source bus 1 is excluded from path-ratio calculations, and a disconnected bus has no finite supply path.

The reverse-flow risk coefficient of bus i in period t is defined as

$$\omega_{i,t}^{\mathrm{rev}} = \frac{P_{i,t}^{+}}{P_i^{\mathrm{PV,max}}} \chi_{i,t}^{\mathrm{rev}} \tag{6}$$

where $P_i^{\mathrm{PV,max}}$ is the installed PV capacity at bus i.

The nodal overvoltage severity, undervoltage severity, and fault-path variation are defined as

$$\begin{aligned} \eta_{i,t}^{+} &= \frac{\left[v_{i,t}-v^{\max}\right]^{+}}{v^{\max}-v^{\mathrm{ref}}} \\ \eta_{i,t}^{-} &= \frac{\left[v^{\min}-v_{i,t}\right]^{+}}{v^{\mathrm{ref}}-v^{\min}} \\ \eta_{i}^{F} &= \left[k_i^{F}\right]^{+} \end{aligned} \tag{7}$$

where $v_{i,t}$ is the voltage magnitude at bus i in period t; $v^{\max}$ and $v^{\min}$ are the admissible upper and lower voltage limits, respectively; and v^{ref} is the nominal voltage.

Using the nodal violation state, reverse-flow contribution, and path-change coefficient, each energized bus is assigned to exactly one of the high-voltage/reverse-flow, low-voltage/load-transfer, or buffer categories. High-voltage eligibility is evaluated first only to resolve overlaps; disconnected buses are stored in a separate set.

(1) A bus is assigned to the high-voltage reverse-power-flow zone $\boldsymbol{\Omega}_{\mathbf{HV},t}$ if $\eta_{i,t}^{+} > 0$, or if interface reverse loading is excessive and both $\eta_t^{\mathrm{rev}} > 0$ and $\omega_{i,t}^{\mathrm{rev}} > \varepsilon_\omega$. Here, ε_ω is the reverse-flow risk threshold and η_t^{rev} is the interface reverse-loading violation defined in Equation (12). Buses in this zone typically exhibit local voltage rise, substantial surplus PV power, or a large contribution to reverse power flow at the interface. Their control objectives are to reduce voltage, mitigate reverse power flow, and suppress excessive reverse power flow at the interface. Notably, contribution to reverse flow is distinguished from an actual nodal voltage violation.

(2) A bus is assigned to the low-voltage load-transfer zone $\boldsymbol{\Omega}_{\mathbf{LV},t}$ if $\eta_{i,t}^{-} > 0$ and $\eta_i^{\mathrm{F}} > 0$. Any energized bus with an actual undervoltage enters the low-voltage/load-transfer zone unless already assigned to the high-voltage category. A longer post-fault path remains a physical explanation and ranking indicator, but is not a prerequisite that could incorrectly place an undervoltage bus in the buffer.

(3) All remaining buses form the safety buffer zone $\boldsymbol{\Omega}_{\mathbf{B},t}$. Disconnected buses are reported separately, fixed to zero voltage/dispatch in the formulation, masked in plots, and excluded from energized-bus voltage statistics.

To avoid uncoordinated resource activation, buses in each risk zone are ranked. For the high-voltage reverse-power-flow zone, the priority vector is

$$\mathbf{I}_{i,t}^{HV} = \left(\eta_{i,t}^{+}, \omega_{i,t}^{rev}, \mu_i\right) \tag{8}$$

where μ_i is the nodal-importance coefficient, which can be assigned according to load class or customer criticality.

For the low-voltage load-transfer zone, the priority vector is

$$\mathbf{I}_{i,t}^{LV} = (\eta_{i,t}^{-}, \eta_i^{F}, \mu_i) \tag{9}$$

The vectors are compared lexicographically: the first component is compared first, followed by the second component if the first components are equal, and so forth.

2.2. Candidate Regulation-Resource Screening for Voltage-Risk Zones

After post-fault risk zoning and nodal prioritization, the regulation resources eligible for subsequent optimization must be determined. Because reconfiguration changes flow directions, voltage profiles, and resource sensitivities, the candidate set is updated with the current topology and operating point. Ignoring regulation direction and zone applicability can admit ineffective or adverse resource actions, increasing computational burden and potentially degrading voltage control. Accordingly, the proposed screening method considers resource sensitivities, zone-specific voltage needs, feasible operating regions, and unit regulation cost under the current topology.

Let $\boldsymbol{\Omega}_{\mathbf{R}}$ denote the set of regulation resources, including OLTCs, CBs, SVGs, PV inverters, SOPs, and distributed energy storage. Because a single resource may produce different voltage responses in different directions, the candidate object is defined as a resource-regulation-direction combination (r,d), where $d \in \boldsymbol{\Omega}_r^d$ is a feasible regulation direction of resource r.

At the topology and operating point of outer iteration k, the voltage change at bus i caused by a unit adjustment of combination (r,d) is

$$\Delta U_{i,t}^{r,d} = S_{i,r,t}^{\mathrm{P,F}} \Delta P_{r,t}^{\mathrm{unit},d} + S_{i,r,t}^{\mathrm{Q,F}} \Delta Q_{r,t}^{\mathrm{unit},d} \tag{10}$$

where $S_{i,r,t}^{\mathrm{P,F}}$ and $S_{i,r,t}^{\mathrm{Q,F}}$ are the post-fault sensitivities of the voltage magnitude at bus i to the active and reactive power adjustment of resource r, respectively; $\Delta P_{r,t}^{\mathrm{unit},d}$ and $\Delta Q_{r,t}^{\mathrm{unit},d}$ are the corresponding unit adjustments in direction d.

For discrete resources such as OLTCs and CBs, a unit adjustment corresponds to one tap movement or one capacitor-step switching action, respectively.

The effect of combination (r,d) on the reverse loading ratio at the upstream-grid interface is

$$\Delta \rho_t^{\mathrm{rev},r,d} = S_{0,r,t}^{\rho,\mathrm{P,F}} \Delta P_{r,t}^{\mathrm{unit},d} \tag{11}$$

where $S_{0,r,t}^{\rho \mathrm{PF}}$ is the finite-difference sensitivity of reverse loading at source bus 1 to the active-power component of direction (r,d) in period t. Source, resource, direction, and period indices are used consistently. For a purely reactive resource whose effect on interface reverse loading is negligible, this term may be set to zero.

In the high-voltage reverse-power-flow zone, control should reduce both nodal voltage and interface reverse loading. The unit regulation benefit of combination (r,d) is therefore defined as

$$\begin{aligned} B_{r,d,t}^{\mathrm{HV}} &= w_{\mathrm{V}} \sum_{i \in \boldsymbol{\Omega}_{\mathbf{HV},t}} \eta_{i,t}^{+} \left[-\Delta U_{i,t}^{r,d} \right]^{+} + w_{\rho} \eta_t^{\mathrm{rev}} \left[-\Delta \rho_t^{\mathrm{rev},r,d} \right]^{+} \\ \eta_t^{\mathrm{rev}} &= \frac{\left[\rho_t^{\mathrm{rev}} - \rho^{\mathrm{rev,max}} \right]^{+}}{\rho^{\mathrm{rev,max}}} \end{aligned} \tag{12}$$

where w_{V} and w_{ρ} weight the mitigation of nodal voltage violations and interface reverse loading, respectively; ρ_t^{rev} is the interface reverse loading ratio in period t; and $\rho^{\mathrm{rev,max}}$ is its admissible upper limit.

In the low-voltage load-transfer zone, the objective is to raise nodal voltage. The unit regulation benefit of combination (r,d) is thus defined as

$$B_{r,d,t}^{\mathrm{LV}} = w_V \sum_{i \in \boldsymbol{\Omega}_{\mathbf{LV},t}} \eta_{i,t}^{-} \left[\Delta U_{i,t}^{r,d} \right]^{+} \tag{13}$$

Let $C_{r,d}^{\mathrm{unit}}$ be the unit regulation cost of combination (r,d). Depending on the device, it may include life-cycle action cost, operation and maintenance cost, energy cost, PV curtailment penalty, storage-loss cost, or load-shedding penalty. For a combination with positive benefit, the unit voltage-regulation cost-benefit ratio is

$$\begin{aligned} \Lambda_{r,d,t}^{\mathrm{HV}} &= \frac{C_{r,d}^{\mathrm{unit}}}{B_{r,d,t}^{\mathrm{HV}}}, \; B_{r,d,t}^{\mathrm{HV}} > 0 \\ \Lambda_{r,d,t}^{\mathrm{LV}} &= \frac{C_{r,d}^{\mathrm{unit}}}{B_{r,d,t}^{\mathrm{LV}}}, \; B_{r,d,t}^{\mathrm{LV}} > 0 \end{aligned} \tag{14}$$

Because Λ is the ratio of unit cost to unit regulation benefit, a smaller Λ indicates that a resource provides more effective voltage regulation at lower cost and should receive higher dispatch priority.

After resource feasibility is considered, high- and low-risk lists are ranked by ascending cost-to-positive-benefit ratio. Ties are resolved by the fixed direction. The final allowable set is the union $\boldsymbol{\Omega}_{\mathrm{t}}^{\mathrm{allow}} = \boldsymbol{\Omega}_{\mathrm{R,t}}^{\mathrm{HV}} \cup \boldsymbol{\Omega}_{\mathrm{R,t}}^{\mathrm{LV}}$, and a direction is excluded only when it is absent

from this union. The 24-direction limit is applied to the overall union, not independently per period or zone. The supplied implementation also preserves a small set of storage-charging, PV-curtailment, reactive-absorption, and OLTC-lowering directions. Specifically, the candidate sets for the high-voltage reverse-power-flow and low-voltage load-transfer zones are

$$\begin{aligned} \boldsymbol{\Omega}_{R,t}^{\mathrm{HV}} &= \left\{ (r,d) \mid r \in \boldsymbol{\Omega}_{\mathrm{R}}, d \in \boldsymbol{\Omega}_{r}^{d}, B_{r,d,t}^{HV} > 0, (r,d) \in F_{r,t} \right\} \\ \boldsymbol{\Omega}_{R,t}^{\mathrm{LV}} &= \left\{ (r,d) \mid r \in \boldsymbol{\Omega}_{\mathrm{R}}, d \in \boldsymbol{\Omega}_{r}^{d}, B_{r,d,t}^{LV} > 0, (r,d) \in F_{r,t} \right\} \end{aligned} \tag{15}$$

where $F_{r,t}$ denotes the feasible regulation-direction set and operating constraints of resource r in period t.

As indicated by Equation (14), candidate screening depends on both the physical effect of a resource on the risk zone and its current availability and regulation cost. For the high-voltage reverse-power-flow zone, candidate resources are ranked in ascending order of $\Lambda_{r,d,t}^{\mathrm{HV}}$, whereas for the low-voltage load-transfer zone, candidate resources are ranked in ascending order of $\Lambda_{r,d,t}^{\mathrm{LV}}$. The ranking determines which candidate resource–regulation-direction combinations are admitted to the subsequent optimization, thereby reducing ineffective variables and improving computational efficiency and zone-specific voltage control.

3. Distribution-Network Voltage Optimization with Fault Reconfiguration and Multi-Resource Coordination

Building on the post-fault risk zones and candidate sets in Section 2, this section formulates a distribution-network voltage optimization model that coordinates network reconfiguration with multiple regulation resources. Over the fault duration, the model seeks safe and economical operation. Its decision variables include branch-switch states, load-restoration ratios, SOP port active and reactive powers, storage charging and discharging powers and state of charge, PV curtailment, and inverter reactive power. The constraints cover fault isolation, radial operation, nodal power balance, branch flows, voltage security, reverse loading at the upstream-grid interface, SOP capacity, energy-storage operation, and PV-inverter capability. An outer iteration updates risk zones and candidate sets as the topology and operating point change; within each optimization solve, the candidate set determined from the current state is treated as fixed.

3.1. Optimization Objectives

Post-fault operation has a clear priority structure. Non-faulted loads should first be restored as far as possible. Once the restoration level is fixed, voltage violations in the high-voltage reverse-power-flow and low-voltage load-transfer zones, together with excessive interface reverse loading, should be minimized. Finally, PV curtailment, network loss, and device operating costs should be reduced without degrading the first two objectives. A three-level lexicographic objective is therefore adopted:

$$\overset{lex}{\min}(F_{\mathrm{L}}, F_{\mathrm{V}}, F_{\mathrm{C}}) \tag{16}$$

where F_{L}, F_{V}, and F_{C} denote the post-fault unserved-load objective, the voltage and interface violation objective, and the operating cost objective, respectively.

The first-level objective minimizes post-fault unserved load:

$$\min F_{\mathrm{L}} = \sum_{t \in \boldsymbol{\Omega}_{\mathrm{T}}^{\mathrm{F}}} \sum_{i \in \boldsymbol{\Omega}_{\mathrm{N}}} \mu_i (1 - \alpha_{i,t}) P_{i,t}^{\mathrm{L}} \Delta t \tag{17}$$

where $\alpha_{i,t}$ is the load-restoration ratio at bus i in period t; $P_{i,t}^{\mathrm{L}}$ is the active load; Δt is the scheduling interval; and μ_i is the load importance coefficient assigned according to load class. Solving the first-level model yields the minimum unserved load value F_{L}^{*}.

With the restoration level fixed by the first level, the second level minimizes nodal voltage violations and excessive reverse loading at the upstream-grid interface. Based on the risk zones identified in Section 2, the overvoltage and undervoltage weights are defined as

$$\begin{aligned} \beta_{i,t}^{+} &= 1 + \beta_{\mathrm{H}} \mathbf{1}_{\{i \in \boldsymbol{\Omega}_{\mathbf{HV},t}\}} \\ \beta_{i,t}^{-} &= 1 + \beta_{\mathrm{L}} \mathbf{1}_{\{i \in \boldsymbol{\Omega}_{\mathbf{LV},t}\}} \end{aligned} \tag{18}$$

where $1\{i \in \boldsymbol{\Omega}_{\mathbf{HV},t}\}$ and $1\{i \in \boldsymbol{\Omega}_{\mathbf{LV},t}\}$ are indicator functions, and β_{H} and β_{L} are risk weighting coefficients for the high-voltage and low-voltage zones, respectively.

The second-level objective minimizes post-fault voltage violations and excessive interface reverse loading:

$$\begin{aligned} &\min F_{\mathrm{V}} = \sum_{t \in \boldsymbol{\Omega}_{\mathbf{T}}^{\mathbf{F}}} \sum_{i \in \boldsymbol{\Omega}_{\mathbf{N}}} \left(\beta_{i,t}^{+} \varepsilon_{i,t}^{+} + \beta_{i,t}^{-} \varepsilon_{i,t}^{-} \right) + \beta_{\rho} \sum_{t \in \boldsymbol{\Omega}_{\mathbf{T}}^{\mathbf{F}}} \zeta_{t}^{\mathrm{rev}} \\ &F_{\mathrm{L}} \le F_{\mathrm{L}}^{*} \end{aligned} \tag{19}$$

where $\varepsilon_{i,t}^{+}$ and $\varepsilon_{i,t}^{-}$ are the normalized overvoltage and undervoltage violations at bus i; ζ_{t}^{rev} is the interface reverse-loading violation; and β_{ρ} is its weighting coefficient. Solving the second-level model yields the minimum violation value F_{V}^{*}.

The third-level objective minimizes post-fault operating cost:

$$F_{\mathrm{C}} = \sum_{t \in \boldsymbol{\Omega}_{\mathbf{T}}^{\mathbf{F}}} \left[\begin{array}{l} c_{\mathrm{PV}} \sum\limits_{i \in \boldsymbol{\Omega}_{\mathbf{PV}}} P_{i,t}^{\mathrm{cur}} \Delta t + c_{\mathrm{loss}} \sum\limits_{(i,j) \in \boldsymbol{\Omega}_{\mathbf{L}}} r_{ij} l_{ij,t} \Delta t \\ + c_{\mathrm{ES}} \sum\limits_{e \in \boldsymbol{\Omega}_{\mathbf{ES}}} \left(P_{e,t}^{\mathrm{ch}} + P_{e,t}^{\mathrm{dis}} \right) \Delta t \\ + c_{\mathrm{SOP}} \sum\limits_{s \in \boldsymbol{\Omega}_{\mathbf{SOP}}} \sum\limits_{p \in \boldsymbol{\Omega}_{s}^{\mathbf{port}}} \left(\left| P_{s,p,t}^{\mathrm{SOP}} \right| + \left| Q_{s,p,t}^{\mathrm{SOP}} \right| \right) \Delta t \\ + c_{\mathrm{QPV}} \sum\limits_{i \in \boldsymbol{\Omega}_{\mathbf{PV}}} \left| Q_{i,t}^{\mathrm{PV}} \right| \Delta t \\ + c_{\mathrm{SVG}} \sum\limits_{g \in \boldsymbol{\Omega}_{\mathbf{SVG}}} \left| Q_{g,t}^{\mathrm{SVG}} \right| \Delta t \\ + \sum\limits_{(i,j) \in \boldsymbol{\Omega}_{\mathbf{SW}}} c_{ij}^{\mathrm{SW}} u_{ij,t}^{\mathrm{SW}} \\ + \sum\limits_{c \in \boldsymbol{\Omega}_{\mathbf{C}}} c_{c}^{\mathrm{C}} u_{c,t}^{\mathrm{C}} + \sum\limits_{o \in \boldsymbol{\Omega}_{\mathbf{OLTC}}} c_{o}^{\mathrm{OLTC}} u_{o,t}^{\mathrm{OLTC}} \end{array} \right] \tag{20}$$

where c_{PV} is the unit PV curtailment cost and $P_{i,t}^{\mathrm{cur}}$ is curtailed PV power; c_{loss} is the unit loss cost, r_{ij} is branch resistance, and $l_{ij,t}$ is squared branch current magnitude; c_{ES} is the unit storage charging/discharging cost and $P_{e,t}^{\mathrm{ch}}$ and $P_{e,t}^{\mathrm{dis}}$ are charging and discharging powers; c_{SOP} is the unit SOP regulation cost and $P_{s,p,t}^{\mathrm{SOP}}$ and $Q_{s,p,t}^{\mathrm{SOP}}$ are the active and reactive powers of port p; c_{QPV} is the unit PV inverter reactive power cost and $Q_{i,t}^{\mathrm{PV}}$ is inverter reactive power; c_{SVG} is the unit SVG regulation cost and $Q_{g,t}^{\mathrm{SVG}}$ is SVG reactive power; $u_{ij,t}^{\mathrm{SW}}$, $u_{c,t}^{\mathrm{C}}$, and $u_{o,t}^{\mathrm{OLTC}}$ are the switching-action variables of switches, CBs, and OLTCs; and c_{ij}^{SW}, c_{c}^{C}, and c_{o}^{OLTC} are their per-action costs. $\boldsymbol{\Omega}_{\mathbf{PV}}$, $\boldsymbol{\Omega}_{\mathbf{ES}}$, $\boldsymbol{\Omega}_{\mathbf{SOP}}$, $\boldsymbol{\Omega}_{\mathbf{SVG}}$, $\boldsymbol{\Omega}_{\mathbf{SW}}$, $\boldsymbol{\Omega}_{\mathbf{C}}$, and $\boldsymbol{\Omega}_{\mathbf{OLTC}}$ are the sets of PV units, storage units, SOPs, SVGs, controllable switches, CBs, and OLTCs, respectively.

The first- and second-level optima are retained through the following locking constraints:

$$\begin{aligned} F_{\mathrm{L}} &\le F_{\mathrm{L}}^{*} \\ F_{\mathrm{V}} &\le F_{\mathrm{V}}^{*} \end{aligned} \tag{21}$$

3.2. Constraints

(1) Fault isolation and network reconfiguration

Following feeder disconnection, every faulted branch remains open to ensure fault isolation:

$$z_{ij,t} = 0, \ (i,j) \in \boldsymbol{\Omega}_{\mathbf{F}}, t \in \boldsymbol{\Omega}_{\mathbf{T}}^{\mathbf{F}} \tag{22}$$

where $z_{ij,t}$ is the operating state of branch (i,j) in period t, with $z_{ij,t} = 1$ for an energized branch and $z_{ij,t} = 0$ for an open branch.

For controllable switched branches,

$$z_{ij,t} \in \{0,1\},\ (i,j) \in \boldsymbol{\Omega}_{\mathbf{SW}} \tag{23}$$

The switching-action variable satisfies

$$\begin{aligned} u^{\mathrm{SW}}_{ij,t} &\geq z_{ij,t} - z_{ij,t-1} \\ u^{\mathrm{SW}}_{ij,t} &\geq z_{ij,t-1} - z_{ij,t} \end{aligned} \tag{24}$$

(2) Radiality constraints

The reconfigured distribution network must remain radial. Let $y_{i,t}$ be the supply state variable of bus i, with $y_{i,t} = 1$ if the bus is energized and $y_{i,t} = 0$ otherwise. A branch can be energized only when both terminal buses are supplied:

$$\begin{cases} z_{ij,t} \leq y_{i,t} \\ z_{ij,t} \leq y_{j,t} \end{cases},\ (i,j) \in \boldsymbol{\Omega}_{\mathbf{L}} \tag{25}$$

For a single-source radial distribution network, the number of energized branches satisfies

$$\sum_{(i,j)\in\boldsymbol{\Omega}_{\mathbf{L}}} z_{ij,t} = \sum_{i\in\boldsymbol{\Omega}_{\mathbf{N}}} y_{i,t} - 1 \tag{26}$$

To ensure connectivity and exclude unintended islands, a virtual-flow variable $f_{ij,t}$ is introduced:

$$\begin{cases} -Mz_{ij,t} \leq f_{ij,t} \leq Mz_{ij,t} \\ \sum\limits_{k:(k,i)\in\boldsymbol{\Omega}_{\mathbf{L}}} f_{ki,t} - \sum\limits_{j:(i,j)\in\boldsymbol{\Omega}_{\mathbf{L}}} f_{ij,t} = y_{i,t},\ i \in \boldsymbol{\Omega}_{\mathbf{N}}\backslash\{0\} \\ \sum\limits_{j:(0,j)\in\boldsymbol{\Omega}_{\mathbf{L}}} f_{0j,t} - \sum\limits_{k:(k,0)\in\boldsymbol{\Omega}_{\mathbf{L}}} f_{k0,t} = \sum\limits_{i\in\boldsymbol{\Omega}_{\mathbf{N}}\backslash\{0\}} y_{i,t} \end{cases} \tag{27}$$

where bus 0 is the main source bus, and M is a sufficiently large positive constant.

(3) Load-restoration constraint

The load-restoration ratio satisfies

$$0 \leq \alpha_{i,t} \leq y_{i,t},\ i \in \boldsymbol{\Omega}_{\mathbf{N}}, t \in \boldsymbol{\Omega}^{\mathbf{F}}_{\mathbf{T}} \tag{28}$$

(4) Branch-flow constraints

The high-fidelity formulation uses the DistFlow model. Let $P_{ij,t}$ and $Q_{ij,t}$ be the active and reactive powers on branch (i,j), $U_{i,t}$ the squared voltage magnitude at bus i, and $l_{ij,t}$ the squared current magnitude. The nodal power balance equations are [30]:

$$\begin{aligned} \sum_{k:(k,i)\in\boldsymbol{\Omega}_{\mathbf{L}}} (P_{ki,t} - r_{ki}l_{ki,t}) + P^{\mathrm{inj}}_{i,t} &= \sum_{j:(i,j)\in\boldsymbol{\Omega}_{\mathbf{L}}} P_{ij,t} \\ \sum_{k:(k,i)\in\boldsymbol{\Omega}_{\mathbf{L}}} (Q_{ki,t} - x_{ki}l_{ki,t}) + Q^{\mathrm{inj}}_{i,t} &= \sum_{j:(i,j)\in\boldsymbol{\Omega}_{\mathbf{L}}} Q_{ij,t} \end{aligned} \tag{29}$$

where $P^{\mathrm{inj}}_{i,t}$ and $Q^{\mathrm{inj}}_{i,t}$ are the active and reactive net injections at bus i. In the implemented balance, positive $P^{\mathrm{inj}}_{i,t}$ denotes import from the upstream grid; PV and ESS discharge are injections, ESS charging and restored demand are withdrawals, and the two lossless SOP ports receive equal and opposite active-power transfers. Reactive signs are defined analogously.

The branch voltage-drop equation is

$$U_{j,t} = U_{i,t} - 2\left(r_{ij}P_{ij,t} + x_{ij}Q_{ij,t}\right) + \left(r^2_{ij} + x^2_{ij}\right)l_{ij,t} \tag{30}$$

With branch switching represented explicitly, Equation (30) can be written using the big-M method as

$$\begin{aligned} &-M(1 - z_{ij,t}) \\ &\leq U_{j,t} - U_{i,t} + 2\left(r_{ij}P_{ij,t} + x_{ij}Q_{ij,t}\right) - \left(r^2_{ij} + x^2_{ij}\right)l_{ij,t} \\ &\leq M(1 - z_{ij,t}) \end{aligned} \tag{31}$$

Branch power, current, and voltage satisfy the second-order-cone relation [31]:

$$P_{ij,t}^2 + Q_{ij,t}^2 \le U_{i,t} l_{ij,t} \tag{32}$$

Branch power and current are also bounded by the branch operating state:

$$\begin{cases} -P_{ij}^{\max} z_{ij,t} \le P_{ij,t} \le P_{ij}^{\max} z_{ij,t} \\ -Q_{ij}^{\max} z_{ij,t} \le Q_{ij,t} \le Q_{ij}^{\max} z_{ij,t} \\ 0 \le l_{ij,t} \le l_{ij}^{\max} z_{ij,t} \end{cases} \tag{33}$$

(5) Nodal voltage-violation constraints

To quantify post-fault voltage violations, introduce overvoltage and undervoltage variables $\varepsilon_{i,t}^+$ and $\varepsilon_{i,t}^-$, which satisfy

$$\begin{cases} U_{i,t} \le (v^{\max})^2 + \Delta U^+ \varepsilon_{i,t}^+ + M(1 - y_{i,t}) \\ U_{i,t} \ge (v^{\min})^2 - \Delta U^- \varepsilon_{i,t}^- - M(1 - y_{i,t}) \\ \varepsilon_{i,t}^+ \ge 0 \\ \varepsilon_{i,t}^- \ge 0 \end{cases} \tag{34}$$

where $v^{\max}$ and $v^{\min}$ are the nodal voltage limits. ΔU^+ and ΔU^- are normalization bases for overvoltage and undervoltage and may be defined as

$$\begin{cases} \Delta U^+ = (v^{\max})^2 - (v^{ref})^2 \\ \Delta U^- = (v^{ref})^2 - (v^{\min})^2 \end{cases} \tag{35}$$

(6) Reverse-loading constraint at the upstream-grid interface

Let $P_{0,t}^{\text{grid}}$ denote the active-power exchange at the upstream-grid interface, with power flowing from the upstream grid into the distribution network defined as positive. The reverse active power P_t^{rev} satisfies

$$\begin{cases} P_{0,t}^{\text{rev}} \ge -P_{0,t}^{grid} \\ P_t^{\text{rev}} \ge 0 \end{cases} \tag{36}$$

Let $S_0^{\max}$ be the interface capacity and $\rho^{\text{rev,max}}$ the permitted reverse loading ratio. To accommodate an unavoidable short-duration violation immediately after a fault, introduce the nonnegative slack variable ξ_t^{rev}. The interface constraint is

$$\begin{cases} P_t^{\text{rev}} \le \rho^{\text{rev,max}} S_0^{\max} + S_0^{\max} \xi_t^{\text{rev}} \\ \xi_t^{\text{rev}} \ge 0 \end{cases} \tag{37}$$

(7) PV active-power curtailment and inverter reactive-power constraints

The actual active PV injection equals the predicted output minus curtailed power:

$$P_{i,t}^{\text{PV,grid}} = P_{i,t}^{\text{PV}} - P_{i,t}^{\text{cur}} \tag{38}$$

PV-inverter reactive power satisfies the apparent-power capability constraint

$$\left(P_{i,t}^{\text{PV,grid}}\right)^2 + \left(Q_{i,t}^{\text{PV}}\right)^2 \le \left(S_i^{\text{PV}}\right)^2 \tag{39}$$

where S_i^{PV} is the rated apparent power of the PV inverter at bus i.

(8) Energy storage constraints

For storage unit e, the charging and discharging powers satisfy

$$\begin{gathered} 0 \le P_{e,t}^{\text{ch}} \le u_{e,t}^{\text{ch}} P_e^{\text{ch,max}} \\ 0 \le P_{e,t}^{\text{dis}} \le u_{e,t}^{\text{dis}} P_e^{\text{dis,max}} \\ u_{e,t}^{\text{ch}} + u_{e,t}^{\text{dis}} \le 1 \\ u_{e,t}^{\text{ch}}, u_{e,t}^{\text{dis}} \in \{0, 1\} \end{gathered} \tag{40}$$

where $u_{e,t}^{\mathrm{ch}}$ and $u_{e,t}^{\mathrm{dis}}$ are the binary charging and discharging state variables.

The state of charge satisfies

$$\begin{aligned} &SOC_{e,t} = SOC_{e,t-1} + \frac{\eta_e^{\mathrm{ch}} P_{e,t}^{\mathrm{ch}} \Delta t}{E_e^{\mathrm{cap}}} - \frac{P_{e,t}^{\mathrm{dis}} \Delta t}{\eta_e^{\mathrm{dis}} E_e^{\mathrm{cap}}} \\ &SOC_e^{\min} \le SOC_{e,t} \le SOC_e^{\max} \\ &SOC_{e,0} = SOC_{e,24} \end{aligned} \tag{41}$$

where $SOC_{e,t}$ is the state of charge; η_e^{ch} and η_e^{dis} are the charging and discharging efficiencies; E_e^{cap} is the rated energy capacity; and $SOC_e^{\min}$ and $SOC_e^{\max}$ are the lower and upper state of charge limits.

(9) SOP constraints

Let Ω_s^{port} denote the set of ports of SOP. For a two-port SOP, active power satisfies

$$P_{s,1,t}^{\mathrm{SOP}} + P_{s,2,t}^{\mathrm{SOP}} + P_{s,t}^{\mathrm{loss}} = 0 \tag{42}$$

where $P_{s,t}^{\mathrm{loss}}$ is the SOP loss.

The apparent power of each SOP port satisfies

$$\left(P_{s,p,t}^{\mathrm{SOP}}\right)^2 + \left(Q_{s,p,t}^{\mathrm{SOP}}\right)^2 \le \left(S_{s,p}^{\mathrm{SOP}}\right)^2 \tag{43}$$

where $S_{s,p}^{\mathrm{SOP}}$ is the rated capacity of port p of SOP s.

(10) SVG reactive-power constraint

SVG reactive power satisfies

$$Q_g^{\mathrm{SVG,min}} \le Q_{g,t}^{\mathrm{SVG}} \le Q_g^{\mathrm{SVG,max}} \tag{44}$$

where $Q_g^{\mathrm{SVG,min}}$ and $Q_g^{\mathrm{SVG,max}}$ are the lower and upper reactive power limits of SVG.

(11) Capacitor-bank constraints

Let q_c^{C} be the reactive-power rating of one step of capacitor bank c and $n_{c,t}^{\mathrm{C}}$ the number of energized steps. Its reactive power output is

$$\begin{cases} Q_{c,t}^{\mathrm{C}} = n_{c,t}^{\mathrm{C}} q_c^{\mathrm{C}} \\ 0 \le n_{c,t}^{\mathrm{C}} \le N_c^{\mathrm{C}} \end{cases} \tag{45}$$

where N_c^{C} is the maximum number of capacitor steps. The CB action variable satisfies

$$\begin{aligned} &u_{c,t}^{\mathrm{C}} \ge n_{c,t}^{\mathrm{C}} - n_{c,t-1}^{\mathrm{C}} \\ &u_{c,t}^{\mathrm{C}} \ge n_{c,t-1}^{\mathrm{C}} - n_{c,t}^{\mathrm{C}} \\ &u_{c,t}^{\mathrm{C}} \ge 0 \end{aligned} \tag{46}$$

The number of CB actions is constrained by

$$\sum_{t \in \boldsymbol{\Omega}_{\mathrm{T}}^{\mathrm{F}}} u_{\mathrm{c,t}}^{\mathrm{C}} \le N_c^{\mathrm{act,max}} \tag{47}$$

where $N_c^{\mathrm{act,max}}$ is the maximum number of CB actions during the fault duration.

(12) OLTC constraints

Let $n_{o,t}^{\mathrm{OLTC}}$ denote the tap position of OLTC. Its turns ratio is

$$\begin{cases} \tau_{o,t} = \tau_o^0 + \Delta\tau_o n_{o,t}^{\mathrm{OLTC}} \\ n_o^{\min} \le n_{o,t}^{\mathrm{OLTC}} \le n_o^{\max} \end{cases} \tag{48}$$

where τ_o^0 is the base turns ratio, $\Delta\tau_o$ is the per-tap step, and $n_o^{\min}$ and $n_o^{\max}$ are the lower and upper tap limits.

The OLTC action variable satisfies

$$\begin{aligned} u_{o,t}^{\mathrm{OLTC}} &\geq n_{o,t}^{\mathrm{OLTC}} - n_{o,t-1}^{\mathrm{OLTC}} \\ u_{o,t}^{\mathrm{OLTC}} &\geq n_{o,t-1}^{\mathrm{OLTC}} - n_{o,t}^{\mathrm{OLTC}} \end{aligned} \tag{49}$$

The number of tap operations is constrained by

$$\sum_{t \in \boldsymbol{\Omega}_{\mathrm{T}}^{\mathrm{F}}} u_{o,t}^{\mathrm{OLTC}} \leq N_{o}^{\mathrm{act,max}} \tag{50}$$

where $N_{o}^{\mathrm{act,max}}$ is the maximum number of OLTC actions during the fault duration.

(13) Candidate-resource activation constraint

Only resource-regulation-direction combinations in the candidate set are eligible for post-fault dispatch. The adjustment of any combination outside the candidate set is fixed to zero:

$$\begin{aligned} &\Delta P_{r,d,t} = 0,\ \Delta Q_{r,d,t} = 0, \\ &(r,d) \notin \boldsymbol{\Omega}_{R,t}^{\mathbf{HV}} \cup (r,d) \notin \boldsymbol{\Omega}_{R,t}^{\mathbf{LV}} \end{aligned} \tag{51}$$

A combination within the candidate set must satisfy the feasible operating region of its resource.

3.3. Solution Method

The DistFlow formulation in Section 3.2, with the power–current equality relaxed to the second-order-cone constraint in Equation (32), defines a MISOCP reference model. Exactness of this relaxation depends on the network constraints and objective structure. The present restoration problem permits reverse power flow and operation at the upper voltage limit, while prioritizing load restoration and violation mitigation before operating cost. Consequently, the applicability of standard sufficient conditions for SOCP exactness is not established, and exactness is not assumed.

The numerical implementation adopts a LinDistFlow approximation to coordinate discrete restoration decisions and resource dispatch within a MILP framework. This implementation is an approximate representation of the network rather than an exact reformulation of the MISOCP. Its accuracy must therefore be assessed against nonlinear power flow, independently of SOCP relaxation tightness [32]. With the candidate set fixed, CPLEX solves the three objectives sequentially, retaining the preceding objective values through the prescribed locking constraints. The outer procedure updates the risk zones and candidate directions as the topology and reference operating state change. The solution procedure combines an outer dynamic update with an inner MILP solve. The three objectives are optimized strictly in lexicographic order. The second level minimizes voltage and interface violations within a tolerance band around the first-level optimum, and the third level minimizes operating cost after the first two levels have been locked. The symbolic locking tolerances are denoted by ε_{L} and ε_{V}; their numerical values, together with the risk weights, are specified in Section 4.1 as case-study parameters.

Step 1: Input the feeder-fault location, original topology, branch data, load and PV forecasts, initial storage states, and operating parameters of all regulation resources. Set the maximum outer-iteration count $K_{\max}$ and convergence criteria.

Step 2: Isolate every branch in $\boldsymbol{\Omega}_{\mathbf{F}}$ to form the initial post-fault topology. Set $k = 0$ and run a power flow calculation to obtain initial nodal voltages, branch flows, and the reverse loading ratio at the upstream grid interface.

Step 3: At topology $z(k)$ and operating point $x(k)$, calculate electrical distances, voltage violations, interface reverse loading violation, and resource sensitivities. Identify the high-voltage reverse-power-flow zone, low-voltage load-transfer zone, and safety buffer zone.

Step 4: Screen candidate resource-regulation-direction combinations for the two risk zones using the current zones, sensitivities, feasible operating regions, and unit regulation costs.

Step 5: With the candidate set fixed, formulate and solve the fault-reconfiguration and multi-resource coordination model. Sequentially minimize unserved load, voltage and interface violations, and operating cost to obtain topology $z^{(k+1)}$, the load restoration plan, and the resource dispatch schedule.

Step 6: Update the power flow state and voltage profile. If both the topology and the candidate set are unchanged between successive iterations, or if the objective variation is below the prescribed threshold, terminate and output the restoration and coordinated voltage-control solution. Otherwise, set $k = k + 1$ and return to Step 3.

Each outer iteration records the number of candidate directions, objective values, topology, and solution time. The CPLEX relative MIP gap, per-stage time limit, outer-loop convergence threshold, and $K_{\max}$ are reported in Section 4.1. Figure 1 summarizes the solution procedure.

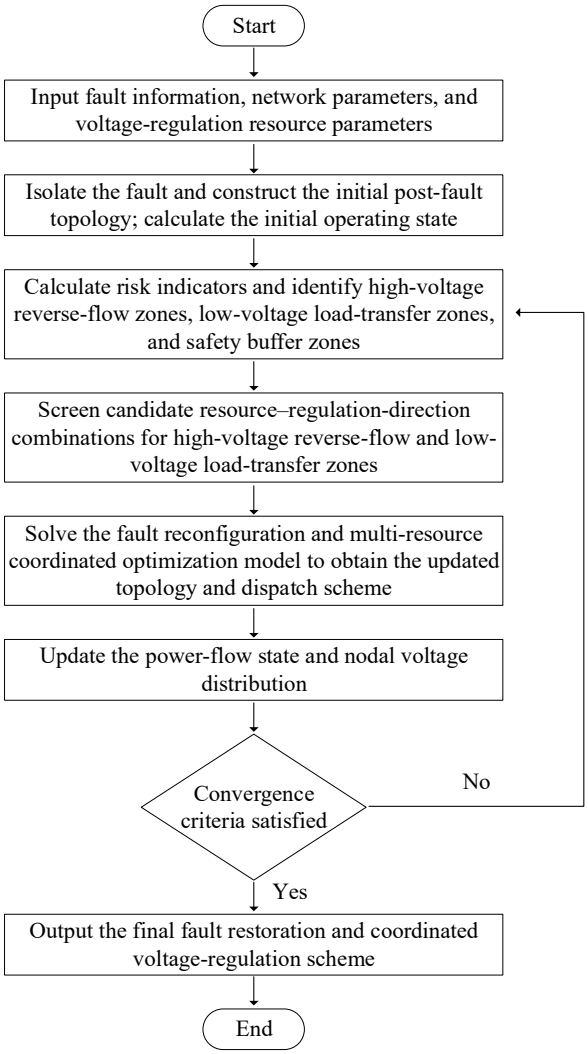


Figure 1. Solution procedure with outer dynamic updates and inner optimization.

4. Results

4.1. Test System and Parameter Settings

(1) System and resource configuration

A modified IEEE 33-bus distribution system [33] was used to evaluate the proposed post-fault voltage-risk zoning, candidate voltage-regulation-resource screening, and coordinated fault-reconfiguration and multi-resource optimization method, as shown in Figure 2. The simulations are conducted in MATLAB 2018a on a 64-bit computer with a 3.0 GHz CPU and 16.0 GB RAM. The optimization models are programmed on the YALMIP platform, and the MISOCP and MILP are solved by the CPLEX 12.10.0 solver.

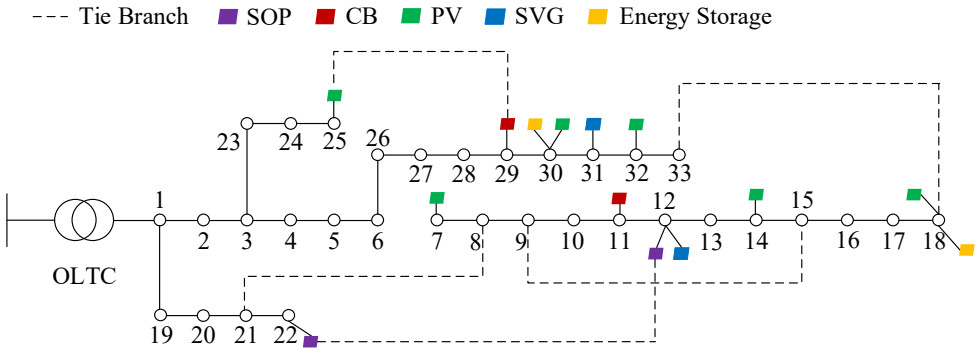


Figure 2. Modified IEEE 33-bus distribution system used in the case study.

The system base power and voltage remain 10 MVA and 12.66 kV, the base active load remains 3.715 MW, branch 6–7 remains the principal feeder-disconnection fault, and the original equipment locations/capacities are unchanged.

Six PV units were connected at buses 7, 14, 18, 25, 30, and 32, with installed capacities of 0.7, 0.95, 0.85, 1, 1.25, and 0.9 MW, respectively. Two-hour energy-storage systems were installed at buses 18 and 30, with rated energies of 1.1 and 1.5 MWh, respectively. A 0.9 MVA soft open point (SOP) connected buses 12 and 22. Static var generators (SVGs) were installed at buses 12 and 31, and capacitor banks were installed at buses 11 and 29. The main transformer was equipped with an on-load tap changer (OLTC) with tap positions from −4 to 4 and a per-tap ratio increment of 0.0125.

(2) Parameter settings

The voltage range is 0.95–1.05 p.u., interface rating 4 MVA, reverse-loading limit 0.25, horizon 24 × 1 h, zoning threshold 0.04. The combined weight assigned to voltage-rise risk and interface reverse-power-flow risk was 0.65. Candidate screening used unit active- and reactive-power adjustments of 0.2 MW and 0.2 Mvar, respectively, and the proposed directional screening retained at most 24 resource-regulation-direction combinations. The three-level lexicographic locking constraints used a combination of an absolute tolerance of 1×10^{-5} and a relative tolerance of 1×10^{-4}. The weights for high-voltage, low-voltage, and interface reverse-power-flow risks were 8, 8, and 10, respectively. The CPLEX relative MIP gap was 1×10^{-4}, the time limit for each optimization level was 180 s, and the maximum number of outer dynamic-update iterations was three. The unit costs of the different voltage-regulation actions are listed in Table 1.

(3) Comparative cases

Three cases were defined to evaluate the candidate voltage-regulation-resource screening method. Case S1 used all-resource optimization, in which every feasible resource-regulation-direction combination participated in a single outer-loop solve. Case S2 applied location-based screening, retaining candidate resources according to their spatial relation to the risk zones without distinguishing the effectiveness of individual regulation directions. Case S3 applied the proposed risk-zone-oriented resource-regulation-direction screening method.

Table 1. Unit cost coefficients of the voltage-regulation actions.

Cost Item	Coefficient	Cost Item	Coefficient	Cost Item	Coefficient
PV curtailment	950	Approximate network loss	15	ESS charge/discharge and reactive-power regulation	35
SOP active/reactive-power regulation	25	PV-inverter reactive-power regulation	8	SVG reactive-power regulation	6
Switching operation	60	Capacitor-bank switching	12	OLTC tap operation	18

Four cases were used to evaluate fault restoration and multi-resource coordinated optimization. Case O1 isolated the fault without network reconfiguration or multi-resource voltage regulation. Case O2 used network reconfiguration alone and did not dispatch multiple types of voltage-regulation resources. Case O3 combined network reconfiguration with static all-resource voltage regulation. Case O4 applied the proposed coordinated method integrating dynamic risk identification, directional screening, and fault reconfiguration.

4.2. Post-Fault Voltage-Risk Zoning Results

After branch 6–7 was opened, buses in each period were assigned to the high-voltage reverse-power-flow zone, low-voltage load-transfer zone, or safety buffer zone according to the current post-fault topology, nodal voltages, surplus PV power, changes in electrical distance, and interface reverse-power-flow sensitivity. Table 2 reports the risk zones and upstream-grid-interface reverse loading ratio for each period, while Figure 3 provides a compact visualization of the 24 h post-fault voltage risk zoning pattern.

Table 2 shows a pronounced intraday migration of the post-fault voltage risks. During periods 1–7, the low-voltage load-transfer zone consistently comprised buses 7–16; in period 8, it contracted to buses 7–9. Low-voltage risk reappeared at buses 7–14 in period 17 and returned to buses 7–16 during periods 18–24. These buses are located downstream of faulted branch 6–7 or within the area affected by load transfer, indicating that the voltage drop caused by the longer supply path is the dominant risk when PV output is low or the transfer path is long.

Table 2. Post-fault 24 h voltage-risk zoning results.

Period (h)	High-Voltage Reverse-Power-Flow Zone	Low-Voltage Load-Transfer Zone	Interface Reverse Loading Ratio
1–7	-	7–16	0
8	-	7–9	0
9	-	-	0
10	-	-	0.1076
11	7, 14, 18, 25, 30, 32	-	0.2682
12	7–18, 25, 30–33	-	0.4652
13	7–18, 25, 30–33	-	0.4458
14	7, 13–15, 18, 25, 30, 32	-	0.37
15	-	-	0.2094
16	-	-	0.0205
17	-	7–14	0
18–24	-	7–16	0

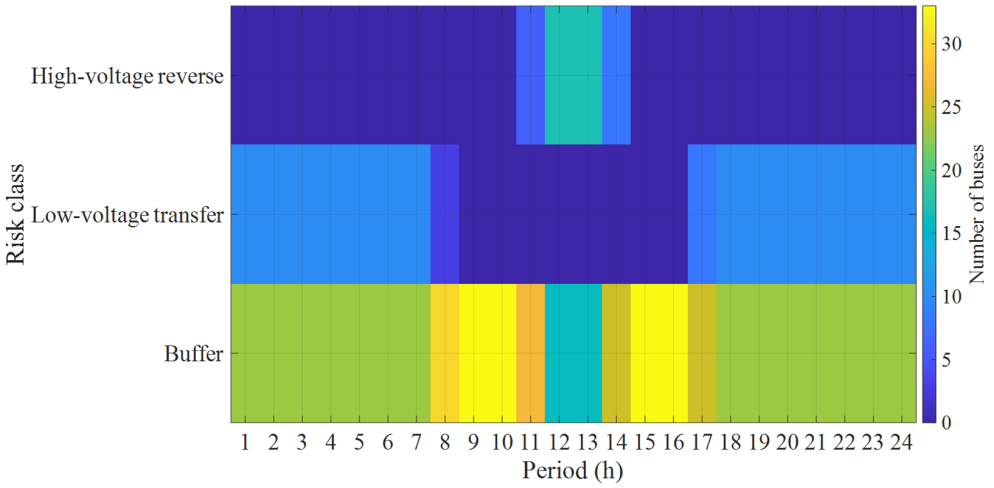


Figure 3. Post-fault voltage-risk zoning over the 24 h scheduling horizon. (The color bar indicates the bus count).

As PV output increased, the dominant risk shifted to high-voltage reverse-power-flow risk during periods 11–14. In period 11, the interface reverse loading ratio reached 0.2682, exceeding the limit of 0.25, and six buses were assigned to the high-voltage reverse-power-flow zone. In period 12, the ratio reached its daily maximum of 0.4652, and the zone expanded to buses 7–18, 25, and 30–33, comprising 17 buses. The same zone persisted in period 13 before contracting to eight buses in period 14. In period 15, the reverse loading ratio fell to 0.2094, below the limit, and no high-voltage reverse-power-flow zone was identified. These results demonstrate a temporal transition from low-voltage load-transfer risk to high-voltage reverse-power-flow risk and then back to low-voltage load-transfer risk as the load-PV balance changes.

4.3. Candidate Voltage-Regulation-Resource Screening Results

To evaluate the proposed resource-regulation-direction screening method, all-resource optimization, location-based screening, and the proposed directional screening strategy were compared. Their final effective model sizes and solution metrics are reported in Table 3.

Table 3. Final effective model size and solution metrics under the candidate-screening strategies.

Case	Direction Combinations	Binary Variables	Continuous Variables	Total Wall Time (s)	Load Restoration Ratio	Cost (p.u.)
S1: All resources	40	1776	7503	261.5	1	203.064
S2: Location screening	38	1776	7479	157.2	1	203.064
S3: Directional screening	24	1752	7263	504.6	1	255.784

Table 3 compares the effects of different screening strategies on model size, load restoration, operating cost, and computational time. All three cases achieve a load recovery ratio of 99.999%. Compared with S1, location-based screening in S2 reduces the candidate directions from 40 to 38 and the continuous variables from 7503 to 7479, while maintaining the same binary-variable count and operating cost. The total wall time decreases from 261.5 to 157.2 s, representing a 39.89% reduction.

Directional screening with dynamic updating in S3 reduces the candidate directions to 24, corresponding to a 40% reduction relative to S1. The binary and continuous variables

decrease from 1776 to 1752 and from 7503 to 7263, respectively, yielding reductions of 1.35% and 3.20%. These smaller reductions arise because screening restricts resource-regulation directions, while the variables required for network topology, branch flows, and multi-period operation remain in the model.

Despite the reduced model size, the operating cost of S3 increases from 203.064 to 255.784, or by 25.96%, and its total wall time increases to 504.6 s. Restricting the candidate set limits the available dispatch combinations, while repeated screening and optimization during dynamic updating introduce additional computational effort. Thus, S3 maintains the same load restoration level with fewer candidate directions, but incurs higher operating cost and total computational time. Section 4.7 further separates the effects of candidate truncation and dynamic updating through matched comparisons.

4.4. Effectiveness of Fault Reconfiguration and Multi-Resource Coordination

Table 4 compares the operating results of the four post-fault strategies. In O1, fault isolation restores only 71.06% of the load, and the minimum voltage of the energized buses is 0.9376 p.u., below the prescribed lower limit of 0.95 p.u. Network reconfiguration in O2 restores all loads but reduces the minimum voltage further to 0.9270 p.u. Meanwhile, the maximum reverse-loading ratio increases from 0.1143 to 0.4652, exceeding the allowable limit of 0.25. These results show that restoring connectivity alone does not ensure acceptable post-fault operation: the reconfigured supply paths and redistributed power flows require additional voltage and reverse-flow regulation.

Table 4. Operating results under the fault-restoration and voltage-regulation strategies.

Case	Load Recovery	Min V	Max V	Reverse Ratio	PV Curtail. (MWh)	Normalized Cost	AC Violations
O1: isolation only	0.7106	0.9376	1.0185	0.1143	0	60	not re-optimized
O2: reconfiguration only	1	0.9270	1.0472	0.4652	0	120	not re-optimized
O3: all-resource	99.999%	0.9535	1.0500	0.2500	0.1440	203.064	none
O4: proposed	99.999%	0.9634	1.0500	0.2500	0.6738	255.784	none

Coordinated resource dispatch in O3 and O4 maintains essentially full load restoration while bringing both voltage and reverse loading within their prescribed limits. The minimum voltages increase to 0.9535 and 0.9634 p.u., respectively, while both cases reach a maximum voltage of 1.0500 p.u. and a reverse-loading ratio of 0.2500. The load recovery ratio of 99.999% is consistent with the lexicographic locking tolerance. Independent nonlinear AC validation reports no voltage or branch-limit violations for either coordinated case.

Compared with O3, O4 raises the minimum voltage by 0.0099 p.u., increasing the margin above the lower voltage limit from 0.0035 to 0.0134 p.u. However, PV curtailment increases from 0.1440 to 0.6738 MWh, and the normalized operating cost rises from 203.064 to 255.784, an increase of 25.96%. Thus, the screened dispatch achieves a higher minimum voltage but requires greater renewable curtailment and operating expenditure. Since both cases attain the same restoration level and satisfy the voltage and reverse-loading limits, the principal difference lies in the resource allocation used to achieve these outcomes. The matched comparisons in Section 4.7 further identify the contributions of candidate truncation and dynamic updating to this difference.

The voltage heatmap further illustrates the spatial and temporal characteristics of O4 in Figure 4. Higher voltages are concentrated at buses 7–18 and 26–33 during hours 10–16, coinciding with high PV output, whereas the lowest-voltage region shifts to buses 7–18 during hours 19–23 as PV generation declines. Together with the voltage-limit compliance reported in Table 4, this pattern shows that the coordinated dispatch accommodates both midday voltage rises and evening voltage depression within the same restoration schedule.

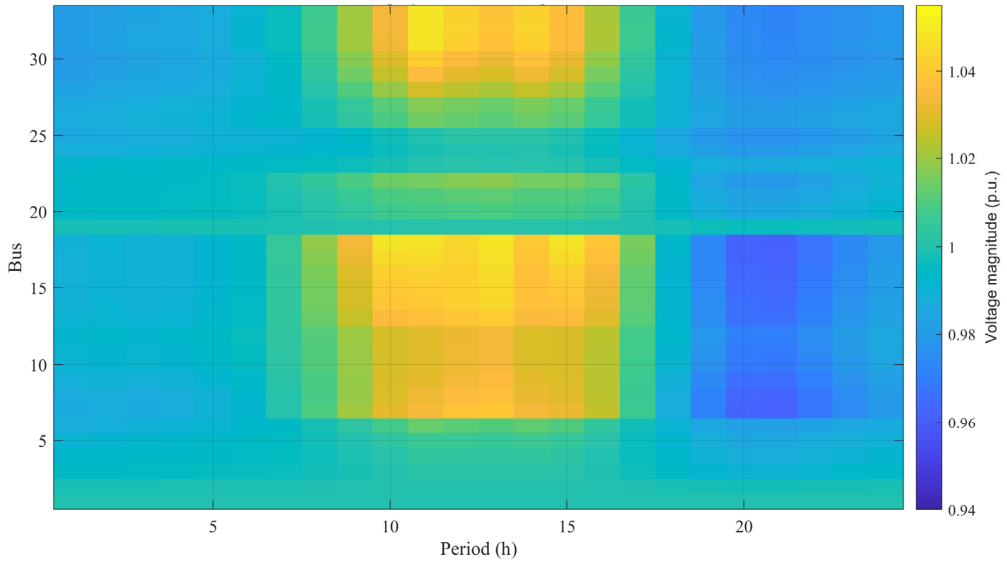


Figure 4. A bus-by-time heatmap of nodal-voltage profiles under the fault-restoration and voltage-regulation strategies.

4.5. Computational Performance

Table 5 compares the model dimensions, outer-iteration counts, and total wall times of the three resource-selection strategies. S1/O3 retains all 40 resource–regulation-direction combinations and uses a single static optimization. S2 applies location-based screening and retains 38 directions. S3/O4 applies directional screening with outer updates and terminates after two iterations when the topology remains unchanged.

Table 5. Model dimensions, outer iterations, and total wall times for the resource-selection strategies.

Case	Outer Iterations	Direction Combinations	Binary Variables	Continuous Variables	Total Wall Time (s)
S1/O3: All-resource static	1	40	1776	7503	261.5
S2: Location-based static	1	38	1776	7479	157.2
S3/O4: Directional dynamic	2	24	1752	7263	504.6

Note: S1 and O3 denote the same all-resource configuration in the screening and operational comparisons, respectively; S3 and O4 denote the proposed directional-screening configuration. Static cases use one optimization pass. S3/O4 terminates after two outer iterations because the topology remains unchanged. The reported times are total wall times, consistent with Table 3.

Location-based screening reduces the number of continuous variables from 7503 to 7479 while retaining 1776 binary variables. Its total wall time decreases from 261.5 to 157.2 s. Directional screening further reduces the candidate set to 24 directions, with 1752 binary variables and 7263 continuous variables. Relative to the all-resource case, these correspond to reductions of 40.0%, 1.35%, and 3.20%, respectively. The smaller reduction in total variables reflects the continued need to represent network operation, restoration decisions, and device constraints after candidate removal.

Despite this reduction in model size, S3/O4 requires 504.6 s, compared with 261.5 s for S1/O3. The outer procedure repeats state assessment, candidate selection, and lexicographic optimization, adding computational work beyond a single static solve. Directional screening therefore reduces the inner-model dimensions but does not reduce total computation time in the principal 33-bus case.

4.6. Twenty-Four-Hour Inputs and Operation of Key Resources

To further explain the risk-mitigation process in Case O4, Figure 5 presents the 24 h load and PV input profiles together with the schedules of the key regulation resources under the proposed method. Table 6 reports representative dispatch results for periods 10–14.

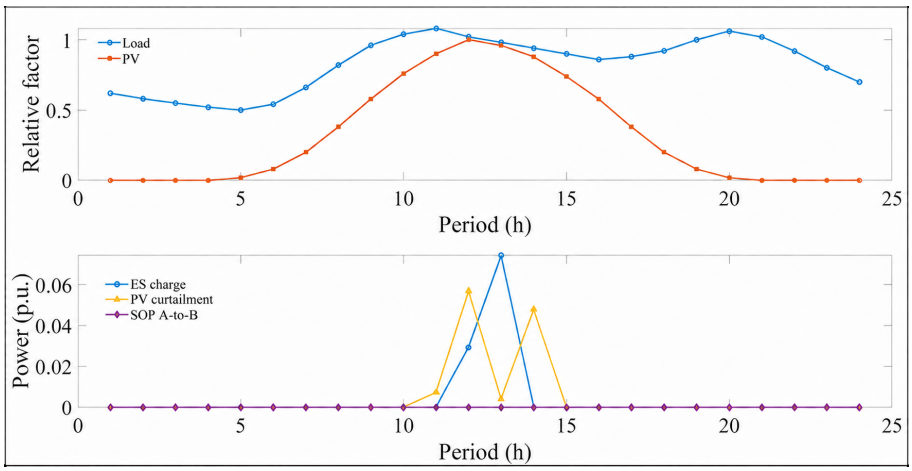


Figure 5. Twenty-four-hour load and PV inputs and operation of key resources under the proposed method.

Table 6. Input profiles and key-resource dispatch around the high reverse-power-flow period.

Period (h)	Load Factor	PV Factor	ESS Charging (p.u.)	PV Curtailment (p.u.)	SOP Active Power A→B (p.u.)	SOP Reactive Power at Terminal B (p.u.)
10	1.04	0.76	0	0	0	0.0098
11	1.08	0.9	0	0.0073	0	0.0434
12	1.02	1	0.0293	0.0568	0	0
13	0.98	0.96	0.0744	0.004	0	0
14	0.94	0.88	0	0.048	0	0

As shown in Figure 5 and Table 6, the system operated in a high-PV-output interval during periods 11–14, with the PV factor reaching 1 in period 12. Correspondingly, PV curtailment and ESS charging were concentrated in these high reverse-power-flow periods. In Case O4, the ESSs charged at 0.0293 and 0.0744 p.u. in periods 12 and 13, respectively, and did not discharge during the 24 h horizon. PV curtailment occurred mainly in periods 11–14, at 0.0073, 0.0568, 0.004, and 0.048 p.u., respectively.

The SOP active-power transfer from terminal A to terminal B remained zero throughout the 24 h horizon, indicating that the SOP did not perform the principal active-power-transfer task in this case study. Its terminal B supplied approximately 0.0098 and 0.0434 p.u. of reactive power in periods 10 and 11, respectively, and remained close to zero in the other periods. Under the adopted resource capacities, candidate directions, and cost coefficients, the dominant active-power measures for mitigating high reverse-power-flow risk were therefore ESS charging and PV curtailment, whereas the SOP provided limited reactive-power support.

4.7. Effects of Candidate Screening, Storage Boundaries, and Operating Conditions

Three additional cases are introduced to distinguish the effects of direction scoring, candidate truncation, and dynamic updating. B1 applies direction scoring without truncation and performs a single static optimization. B2 retains the top 24 directions under the same

static solution procedure. B3 retains all 40 directions and applies the same outer-update procedure as O4. Together with O3 and O4, these cases establish the comparisons reported in Table 7 and Figure 6.

Table 7. Effects of direction scoring, candidate truncation, and dynamic updating.

Case	Candidate/Update Rule	Dirs	Cost	Curtail. MWh	Total s	Stop
B1	direction score; no cap; static	40	203.064	0.1440	247.9	Static single pass
B2	direction score; top-24; static	24	256.588	0.6967	270.1	Static single pass
O4	direction score; top-24; dynamic	24	255.784	0.6738	504.6	Topology unchanged
B3	all 40; dynamic	40	203.064	0.1440	511.9	Topology unchanged

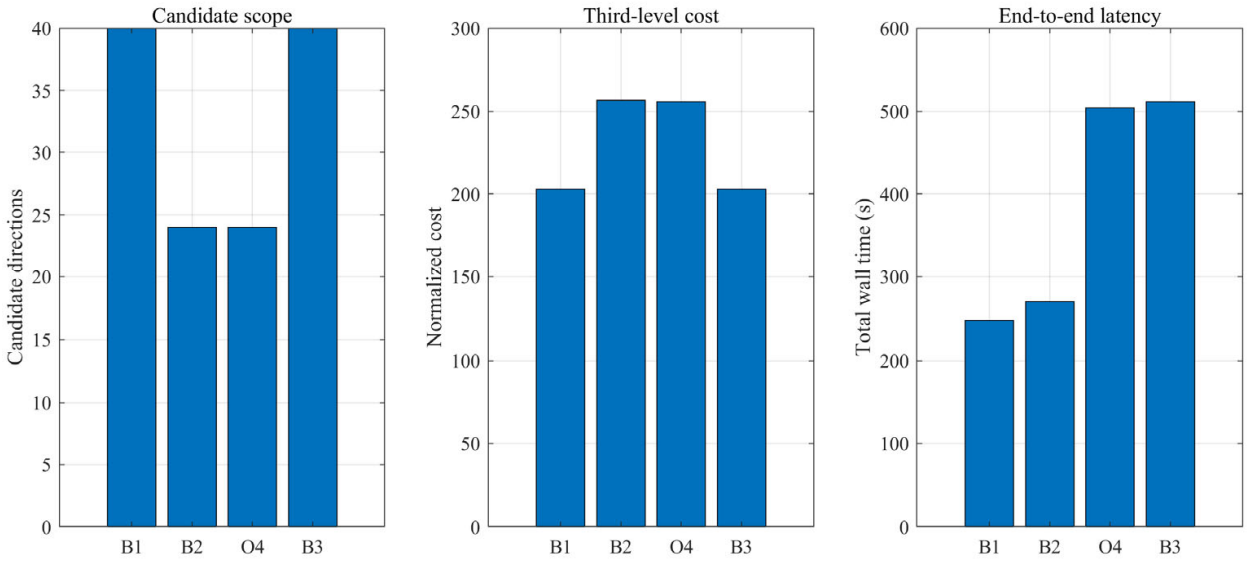


Figure 6. Comparison of candidate counts, operating costs, and total computation times.

B1 retains all 40 directions and reproduces the O3 cost of 203.064 and PV curtailment of 0.1440 MWh. Thus, direction scoring alone does not restrict dispatch in this case. Introducing the top-24 cap in B2 increases the cost to 256.588 and curtailment to 0.6967 MWh. Dynamic updating in O4 reduces these values slightly to 255.784 and 0.6738 MWh, respectively, but increases total computation time from 270.1 to 504.6 s. B3 also reproduces the all-resource operating result while requiring 511.9 s. These comparisons identify candidate truncation as the principal source of the economic penalty. Updating provides a modest improvement within the restricted candidate set, whereas it leaves the unrestricted operating result unchanged.

Building on Table 5, the matched-update comparisons in Table 7 further distinguish model reduction from outer-loop overhead. With all 40 directions retained, B3 requires 511.9 s, compared with 504.6 s for O4. With the top-24 restriction fixed, the static case B2 requires 270.1 s, while dynamic updating in O4 increases the total to 504.6 s. These results show that the computational effect of screening depends on both the candidate restriction and the update procedure.

Table 8 and Figure 7 examine whether the comparison depends on the storage terminal condition. The main cases impose a terminal SOC lower bound, while B4 and B5 impose cyclic SOC conditions on O3 and O4, respectively. Under the cyclic condition, the all-resource cost increases from 203.064 to 205.721, with curtailment unchanged at 0.1440 MWh. In contrast, the screened-case cost increases from 255.784 to 314.929, and curtailment rises

from 0.6738 to 1.3247 MWh. Figure 8 shows the associated charging and discharging schedules returning each ESS to its initial SOC. The stronger response of the screened case indicates that candidate restrictions reduce the flexibility available to reconcile midday surplus absorption with end-of-horizon energy requirements.

Table 8. Operating results under alternative terminal SOC constraints.

Case	Boundary	Cost	Curtail. MWh	Iterations	Termination
O3	emergency lower bound	203.064	0.1440	1	Static single pass
O4	emergency lower bound	255.784	0.6738	2	Topology unchanged
B4/O3	cyclic	205.721	0.1440	1	Static single pass
B5/O4	cyclic	314.929	1.3247	2	Topology unchanged

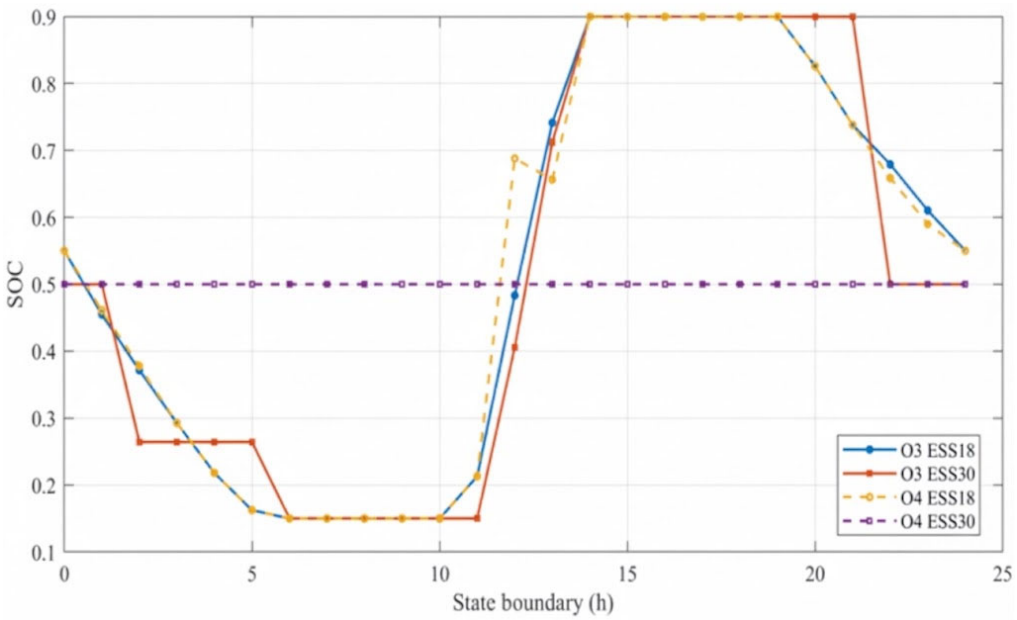


Figure 7. Individual ESS SOC trajectories under cyclic terminal constraints.

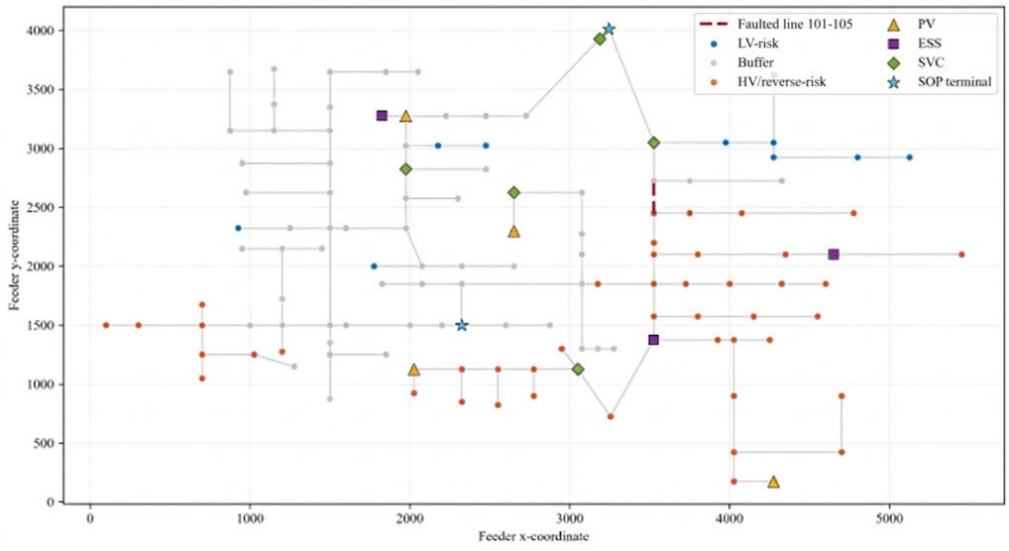


Figure 8. Restored topology, resource locations, and reference-state risk zoning of the IEEE 123-node feeder.

Table 9 further examines the influence of candidate capacity and operating parameters. Retaining 16 directions yields a cost of 328.31 and curtailment of 1.275 MWh, whereas retaining 32 directions reduces these values to 203.09 and 0.144 MWh, approaching the all-resource result. The economic penalty therefore depends strongly on the candidate cap. Halving the PV-curtailment coefficient narrows the cost difference between the all-resource and screened cases, while doubling the ESS coefficient preserves a substantial difference. Halving the SOP coefficient leaves the reported operating results essentially unchanged. Similarly, the tested SOP rating and terminal-location changes do not alter the screened-case cost or curtailment, showing that these adjustments do not relieve the limiting dispatch conditions in the tested scenarios.

Table 9. Sensitivity to candidate caps, cost coefficients, and operating conditions.

Test	Dirs	Recovery	Cost	Curt. MWh	Total s
cap16	16	100.00%	328.31	1.275	137.1
cap32	32	100.00%	203.09	0.144	124.2
PV cost_half_all	40	100.00%	196.22	0.144	114.5
PV cost_half_directional	24	100.00%	223.50	0.697	122.7
ES cost_double_all	40	100.00%	213.46	0.144	115.5
ES cost_double_directional	24	100.00%	263.30	0.697	124.6
SOP cost_half_all	40	100.00%	203.06	0.144	116.7
SOP cost_half_directional	24	100.00%	256.59	0.697	147.9
PV plus10_all	40	100.00%	425.51	2.409	121.1
PV plus10_directional	24	100.00%	499.33	3.065	147.3
ES unavailable_all	40	100.00%	387.80	2.197	144.0
ES unavailable_directional	24	100.00%	496.91	2.197	142.5
Fault 12_13_all	40	100.00%	201.36	0.144	158.1
Fault 12_13_directional	24	100.00%	222.93	0.133	139.4
fault24_25_all	40	100.00%	211.99	0.144	122.3
Fault 24_25_directional	24	100.00%	241.79	0.262	142.9
SOP_0p5MVA_directional	24	100.00%	256.59	0.697	144.8
SOP_1p5MVA_directional	24	100.00%	256.59	0.697	153.0
SOP_7_25_directional	24	100.00%	256.59	0.697	132.3
SOP_18_33_directional	24	100.00%	256.59	0.697	138.2

Changes in PV availability, storage availability, and fault location produce different screening outcomes. Increasing PV availability by 10% raises curtailment to 2.409 and 3.065 MWh in the all-resource and screened cases, respectively. Removing storage increases both values to 2.197 MWh, although their operating costs remain different. For the fault at branch 12–13, the screened case curtails slightly less PV than the all-resource case but still incurs a higher total cost. These results show that curtailment alone does not explain every cost difference; screening also changes the use of other regulation resources.

The component breakdown in Table 10 explains the principal O3–O4 cost difference. The PV-curtailment component increases by 50.330 normalized units, accounting for approximately 95% of the total increase of 52.720. The loss-proxy and SVG components also increase, while the ESS and PV-reactive components decrease. Switching costs remain identical at 120, and the SOP, capacitor, and OLTC components are zero in both cases. The higher O4 cost therefore arises mainly from greater reliance on PV curtailment, with smaller contributions from changes in the remaining dispatch components.

Table 10. Breakdown of normalized operating costs for O3 and O4.

Component	O3	O4
PV Curtailment	13.682	64.012
PV Reactive	16.415	14.630
ESS	10.393	8.273
SOP	0.000	0.000
SVG	15.094	16.490
LossProxy	27.480	32.379
Switching	120.000	120.000
Capacitor	0.000	0.000
OLTC	0.000	0.000
Recomputed Total	203.064	255.784

4.8. Validation on the IEEE 123-Node Feeder

To examine the applicability of resource-direction screening to a larger unbalanced distribution network, an additional 24 h study is conducted on the standard IEEE 123-node feeder using its OpenDSS network data. Following a fault on line 101–105, the normally open switch Sw7 between buses 151 and 300 is closed to restore downstream supply. Four PV groups, three ESS groups, five SVC groups, and one two-terminal SOP are incorporated, providing 40 candidate regulation directions. Figure 8 presents the restored topology, resource locations, and reference-state zoning. The load and PV profiles follow the relative trajectories used in the main study, and each ESS satisfies intertemporal energy constraints and a cyclic terminal SOC condition. The restored topology is held fixed to isolate the effect of screening on continuous resource dispatch. The all-direction and screened LP models use the same operating constraints and objective, with the screened model retaining 24 directions. A zero-export condition is imposed at the source interface. To accommodate discrepancies between the linear model and nonlinear power flow, the optimization uses voltage bounds of 0.953–1.047 p.u. within the admissible range of 0.95–1.05 p.u., together with a 15 kW source-power margin. The optimized device settings are subsequently evaluated hour by hour using three-phase unbalanced nonlinear AC power flow in OpenDSS, covering 274 energized phase nodes.

Figures 9 and 10 show the voltage distribution and operating trajectories before and after coordinated dispatch. The restored baseline exhibits source reverse flow during six high-PV periods and a midday voltage maximum exceeding 1.05 p.u. After regulation, source reverse flow is eliminated, and all 24 hourly AC evaluations converge with voltages within the admissible range. The daily minimum and maximum voltages are 0.95298 and 1.04932 p.u., respectively. PV curtailment totals 2.1843 MWh and is concentrated around the generation peak. The resulting schedules address midday surplus generation while maintaining acceptable voltages during the evening low-voltage interval.

Figure 11 compares the model dimensions and solution times. Screening reduces the candidate directions from 40 to 24 and the 24 h dispatch variables from 960 to 576, both by 40%. The constraint count decreases more modestly, from 13,755 to 13,467, because network operating constraints remain necessary after candidate removal. Following one warm-up solve, each LP is solved ten times on an Intel Core i7-11370H computer with four cores and eight threads. The median LP solution time decreases from 0.342 to 0.182 s, approximately 46.7%. These measurements cover the optimization solve; sensitivity calculation and nonlinear AC validation are timed separately from this metric.

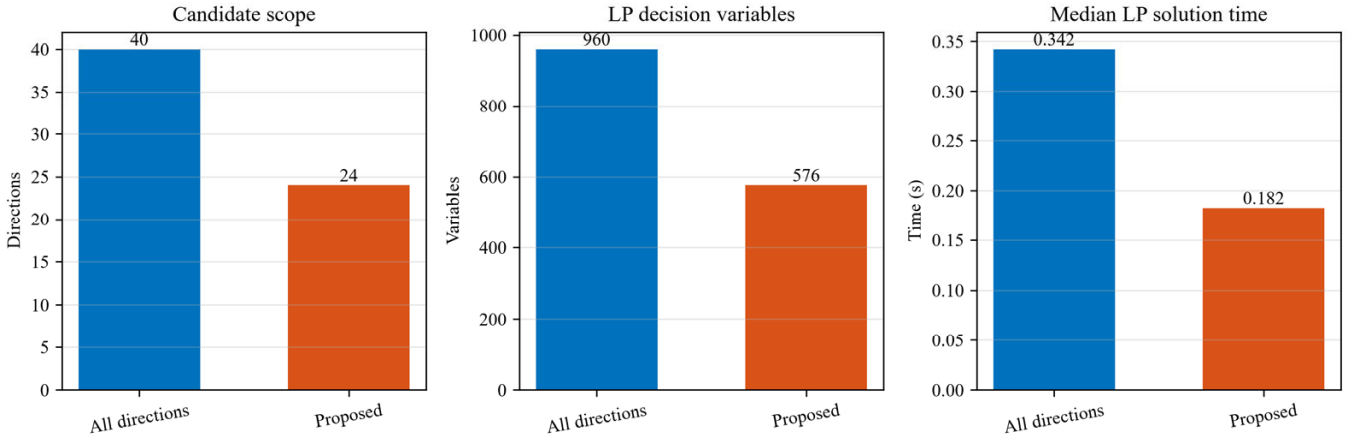


Figure 9. Candidate directions, dispatch variables, and median LP solution times on the IEEE 123-node feeder.

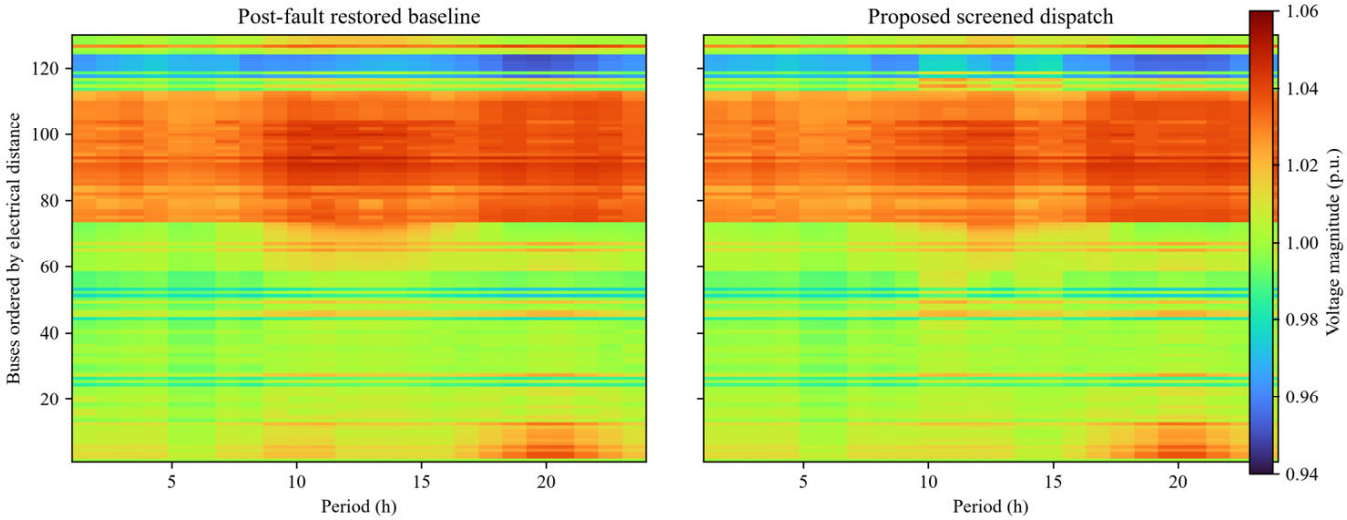


Figure 10. Voltage distributions of the restored baseline and screened dispatch on the IEEE 123-node feeder.

The normalized costs are 2543.155936 for the all-direction model and 2543.156109 for the screened model, a relative difference of approximately 0.0000068%. Unlike the principal 33-node case, the retained directions in this operating condition preserve essentially the same objective value while reducing the dispatch dimension. This contrast supports the candidate-cap analysis in Section 4.7: the economic effect of screening depends on which operating options are excluded, rather than the reduction percentage alone.

The screened schedule produces a peak line current of 624.51 A, compared with 631.44 A at the standard feeder's original operating point. This comparison reports current magnitude relative to the reference operating point; conductor thermal-limit compliance requires separately specified ampacity ratings. Overall, the larger-feeder experiment demonstrates the applicability of the screening and dispatch procedure to an unbalanced network, with verified voltage compliance.

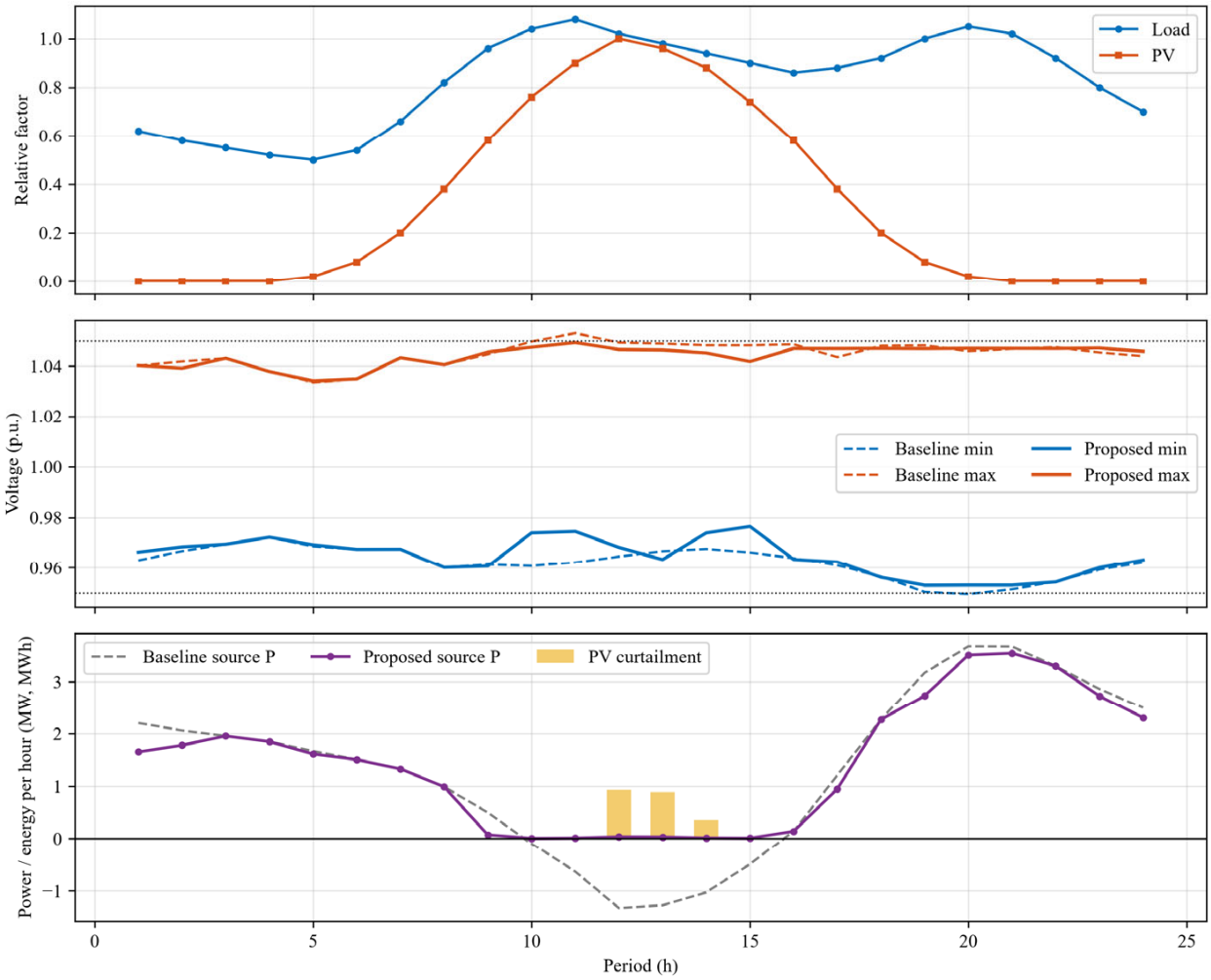


Figure 11. Load and PV profiles, voltage profiles, source power, and PV curtailment on the IEEE 123-node feeder.

5. Discussion

The results highlight the importance of selecting regulation directions according to the post-fault topology and operating state. Regional PV-storage coordination [6], sensitivity-based voltage control [16], and dynamic restoration [9] provide established foundations for coordinating network flexibility. This study connects these principles through risk-dependent resource-direction screening and outer updates. Its contribution lies in this selection mechanism and its interaction with restoration decisions, while the underlying sensitivity calculations, device models, and optimization tools are established methods.

The comparisons show that reducing the candidate set does not necessarily improve operating economy or total computation time. In the principal 33-bus case, screening preserves restoration and modeled constraint compliance but increases cost and curtailment, mainly because truncation excludes economically useful flexibility. Outer updating provides a modest dispatch improvement with additional computational effort. In the fixed-topology 123-node case, the retained directions preserve essentially the same cost while reducing dispatch variables and LP solution time. Screening performance therefore depends on the flexibility retained under the prevailing network and intertemporal constraints.

SOP active transfer has a distinct physical role in this single-source network. It redistributes power internally, influencing local voltages, branch loading, and feasible resource dispatch. With other injections fixed, its effect on aggregate source exchange arises through changes in network and converter losses. ESS charging directly absorbs surplus energy,

and PV curtailment reduces generation. SOP coordination can facilitate these adjustments by relieving local constraints, but internal active transfer itself does not remove aggregate PV surplus. Its zero active transfer in the principal case consequently reflects the tested dispatch conditions rather than a general absence of operational value.

The evidence covers the reported deterministic operating scenarios, with the larger-feeder study limited to dispatch under a fixed restored topology. Nonlinear AC evaluations support the reported operating-point compliance, but do not establish security under untested disturbances or uncertainty. Likewise, shorter LP solution times do not establish faster end-to-end restoration or online performance. Further assessment should address load/PV uncertainty, zoning-parameter sensitivity, adaptive candidate expansion, and complete operational timing.

6. Conclusions

This paper developed a post-fault coordination method that links voltage-risk zoning, resource-direction screening, and restoration optimization. Its contribution is the explicit selection and updating of regulation directions according to the post-fault topology and operating state, using established sensitivity calculations, network models, and lexicographic optimization.

In the modified IEEE 33-bus system, the proposed method retained 24 of 40 candidate directions while achieving 99.999% load restoration and the same modeled voltage and interface-limit compliance as the all-resource case. This reduction increased normalized cost from 203.064 to 255.784, PV curtailment from 0.1440 to 0.6738 MWh, and total wall time from 261.5 to 504.6 s. The additional comparisons identified candidate truncation as the principal source of the economic penalty, with outer updating providing a modest improvement within the restricted set.

In the fixed-topology IEEE 123-node study, screening reduced dispatch variables by 40% and median solution time by approximately 46.7%, with essentially unchanged cost. Hourly nonlinear three-phase evaluations confirmed voltages within 0.95–1.05 p.u. and elimination of source reverse flow for the screened schedule. These results demonstrate that candidate reduction can preserve dispatch quality when the retained directions provide sufficient flexibility.

The demonstrated benefit is a smaller, physically interpretable candidate set whose economic and computational effects depend on the operating conditions. SOP active transfer redistributes power internally and influences local constraints and losses, whereas ESS charging and PV curtailment directly address aggregate PV surplus.

For the distribution system research community and network operators, these findings provide a basis for assessing when resource screening can simplify post-fault coordination without sacrificing useful flexibility. The contrasting feeder results show that screening should be evaluated jointly through restoration performance, operating cost, renewable energy curtailment, and end-to-end computation time, rather than candidate set reduction alone. This insight can inform the design of restoration tools that balance computational tractability with the operational value of distributed resources. Future research should develop adaptive candidate expansion mechanisms that reintroduce excluded regulation directions when the retained set limits feasibility or increases dispatch cost. Further work should examine the robustness of voltage-risk zoning and resource selection to load and PV uncertainty, zoning parameters, and changing network conditions. Validation on larger unbalanced feeders with jointly optimized restoration topology, together with complete timing assessments covering sensitivity calculation, screening, optimization, and nonlinear verification, is also needed to establish practical deployment requirements.

https://doi.org/10.3390/su182111333

Author Contributions: Conceptualization, J.J. and G.L.; methodology, G.L. and F.X.; software, G.L.; validation, J.J., G.L. and Y.G.; formal analysis, G.L.; investigation, J.J. and G.L.; resources, J.J., Y.G. and L.H.; data curation, J.J. and G.L.; writing—original draft preparation, J.J. and G.L.; writing—review and editing, F.X., Y.G. and L.H.; visualization, G.L.; supervision, F.X., Y.G. and L.H.; project administration, J.J. and L.H. All authors have read and agreed to the published version of the manuscript.

Funding: This research was supported by State Grid Jiangsu Electric Power Co., Ltd. Technology Project (J2025144).

Institutional Review Board Statement: Not applicable.

Informed Consent Statement: Not applicable.

Data Availability Statement: The data and code supporting the findings of this study are available from the corresponding author upon reasonable request.

Conflicts of Interest: Authors Jiangping Jing and Ye Guo are employed by the company State Grid Jiangsu Electric Power Co., Ltd. Author Gaige Liang is employed by the company Xuzhou Power Supply Branch of State Grid Jiangsu Electric Power Co., Ltd. The remaining authors declare that the research was conducted in the absence of any commercial or financial relationships that could be construed as a potential conflict of interest.

References

1. Ehsanbakhsh, M.; Sepasian, M.S. Bi-objective robust planning model for optimal allocation of soft open points in active distribution network: A flexibility improvement approach. *Electr. Power Syst. Res.* **2023**, *224*, 109780. [CrossRef]
2. Mardanimajd, K.; Karimi, S.; Anvari-Moghaddam, A. Voltage stability improvement in distribution networks by using soft open points. *Int. J. Electr. Power Energy Syst.* **2024**, *155*, 109582. [CrossRef]
3. Zhang, W.; Sheng, W.; Liu, K.; Kang, T.; Zhan, H. Toward optimal voltage/VAR control with smart PVs in active distribution networks. *Electr. Power Syst. Res.* **2024**, *228*, 110076. [CrossRef]
4. Zhang, B.; Cao, D.; Hu, W.; Ghias, A.M.Y.M.; Chen, Z. Physics-Informed Multi-Agent deep reinforcement learning enabled distributed voltage control for active distribution network using PV inverters. *Int. J. Electr. Power Energy Syst.* **2024**, *155*, 109641. [CrossRef]
5. Wang, Y.; Fu, W.; Chen, J.; Wang, J.; Zhen, Z.; Wang, F.; Xu, F.; Duić, N.; Yang, D.; Lv, Y. Spatiotemporal Federated Learning Based Regional Distributed PV Ultra-Short-Term Power Forecasting Method. *IEEE Trans. Ind. Appl.* **2024**, *60*, 7413–7425. [CrossRef]
6. Wang, J.; Lan, J.; Wang, L.; Lin, Y.; Hao, M.; Zhang, Y.; Xiang, Y.; Qin, L. Voltage Hierarchical Control Strategy for Distribution Networks Based on Regional Autonomy and Photovoltaic-Storage Coordination. *Sustainability* **2024**, *16*, 6758. [CrossRef]
7. Liu, F.; Chen, C.; Lin, C.; Li, G.; Xie, H.; Bie, Z. Utilizing Aggregated Distributed Renewable Energy Sources with Control Coordination for Resilient Distribution System Restoration. *IEEE Trans. Sustain. Energy* **2023**, *14*, 1043–1056. [CrossRef]
8. Konar, S.; Srivastava, A.K.; Dubey, A. Distributed Optimization for Autonomous Restoration in DER-Rich Distribution System. *IEEE Trans. Power Deliv.* **2023**, *38*, 3205–3217. [CrossRef]
9. Carrión, C.E.C.; Faria, W.R.; Macedo, L.H.; Romero, R.; Pereira, B.R. Dynamic Service Restoration of Distribution Networks with Volt-Var Devices, Distributed Energy Resources, and Energy Storage Systems. *IEEE Trans. Sustain. Energy* **2024**, *15*, 903–919. [CrossRef]
10. Yang, X.; Xu, C.; Wen, J.; Zhang, Y.; Wu, Q.; Zuo, W.; Cheng, S. Cooperative Repair Scheduling and Service Restoration for Distribution Systems with Soft Open Points. *IEEE Trans. Smart Grid* **2023**, *14*, 1827–1842. [CrossRef]
11. Wang, K.; Xue, Y.; Zhou, Y.; Li, Z.; Chang, X.; Sun, H. Distributed coordinated reconfiguration with soft open points for resilience-oriented restoration in integrated electric and heating systems. *Appl. Energy* **2024**, *365*, 123207. [CrossRef]
12. Xu, R.; Zhang, C.; Zhang, D.; Yang Dong, Z.; Yip, C. Adaptive Robust Load Restoration via Coordinating Distribution Network Reconfiguration and Mobile Energy Storage. *IEEE Trans. Smart Grid* **2024**, *15*, 5485–5499. [CrossRef]
13. Zhang, W.; Zhang, C.; Li, J.; Cao, S.; Wang, D.; Yang, H.; Du, J.; Shuai, Z. Resilience-oriented comparative study of SOP-based service restoration in distribution systems. *Electr. Power Syst. Res.* **2024**, *228*, 110050. [CrossRef]
14. Li, S.; Li, Z.; Shahidehpour, M.; Huang, W.; Zheng, J.H. Dispatchable region for distributed renewable energy generation in reconfigurable AC–DC distribution networks with soft open points. *Appl. Energy* **2024**, *371*, 123704. [CrossRef]
15. Yang, X.; Jiang, W.; Ma, J.; Xu, D.; Zhang, C.; Yang, Y.; Xu, Z. Flexibility provision by virtual power line and soft open point in AC/DC distribution systems. *Int. J. Electr. Power Energy Syst.* **2025**, *166*, 110528. [CrossRef]
16. Cheng, Z.; Wang, L.; Su, C.; Zhang, R.; Li, X.; Zhang, B. Data-Driven Coordinated Voltage Control Strategy for Distribution Networks with High Proportion of Renewable Energy Based on Voltage–Power Sensitivity. *Sustainability* **2025**, *17*, 4955. [CrossRef]

17. Yang, T.; Cheng, Q.; Bai, S.; Wu, D.; Chen, B.; Lu, D.; Wu, H. Active–Passive Responsibility-Driven Overvoltage Mitigation for Sustainable Distribution Networks with High Distributed Photovoltaic Penetration. *Sustainability* **2026**, *18*, 4705. [CrossRef]
18. Zhao, Y.; Zhang, G.; Hu, W.; Huang, Q.; Chen, Z.; Blaabjerg, F. Meta-Learning Based Voltage Control for Renewable Energy Integrated Active Distribution Network Against Topology Change. *IEEE Trans. Power Syst.* **2023**, *38*, 5937–5940. [CrossRef]
19. Abo Alwez, M.; Jasni, J.; Mohd Radzi, M.A.; Azis, N. Adaptive reactive power control for voltage rise mitigation on distribution network with high photovoltaic penetration. *Renew. Sustain. Energy Rev.* **2025**, *207*, 114948. [CrossRef]
20. Yan, X.; Wang, Q.; Bu, J. High penetration PV active distribution network power flow optimization and loss reduction based on flexible interconnection technology. *Electr. Power Syst. Res.* **2024**, *226*, 109839. [CrossRef]
21. Ebrahimi, H.; Galvani, S.; Talavat, V.; Farhadi-Kangarlu, M. A conditional value at risk based stochastic allocation of SOP in distribution networks. *Electr. Power Syst. Res.* **2024**, *228*, 110111. [CrossRef]
22. Wang, P.; Li, H. Coordinated planning of soft open point and energy store system in active Distribution networks under source-load imbalance. *Electr. Power Syst. Res.* **2024**, *231*, 110324. [CrossRef]
23. Zhang, T.; Mu, Y.; Dong, L.; Jia, H.; Pu, T.; Wang, X. Fully parallel decentralized load restoration in coupled transmission and distribution system with soft open points. *Appl. Energy* **2023**, *349*, 121626. [CrossRef]
24. Meng, L.; Yang, X.; Zhu, J.; Wang, X.; Meng, X. Network partition and distributed voltage coordination control strategy of active distribution network system considering photovoltaic uncertainty. *Appl. Energy* **2024**, *362*, 122846. [CrossRef]
25. Qiao, J.; Mi, Y.; Shen, J.; Xia, D.; Li, D.; Wang, P. Active and reactive power coordination optimization for active distribution network considering mobile energy storage system and dynamic network reconfiguration. *Electr. Power Syst. Res.* **2025**, *238*, 111080. [CrossRef]
26. Bonfiglio, A.; La Fata, A.; Minetti, M. A pattern recognition based tool for smart distribution networks reconfiguration. *Electr. Power Syst. Res.* **2025**, *248*, 111890. [CrossRef]
27. Nebuloni, R.; Ilea, V.; Bovo, C.; Berizzi, A.; Arrigoni, C.; Re, F.; Bonera, R. Optimal reconfiguration of radial distribution networks with renewable energy resources by considering configuration shift steps. *Sustain. Energy Grids Netw.* **2025**, *43*, 101861. [CrossRef]
28. Zhang, Z.; Li, P.; Ji, H.; Zhao, J.; Xi, W.; Wu, J.; Wang, C. Combined central-local voltage control of inverter-based DG in active distribution networks. *Appl. Energy* **2024**, *372*, 123813. [CrossRef]
29. Christakou, K.; LeBoudec, J.Y.; Paolone, M.; Tomozei, D.C. Efficient Computation of Sensitivity Coefficients of Node Voltages and Line Currents in Unbalanced Radial Electrical Distribution Networks. *IEEE Trans. Smart Grid* **2013**, *4*, 741–750. [CrossRef]
30. Baran, M.; Wu, F.F. Optimal sizing of capacitors placed on a radial distribution system. *IEEE Trans. Power Deliv.* **1989**, *4*, 735–743. [CrossRef]
31. Farivar, M.; Low, S.H. Branch Flow Model: Relaxations and Convexification—Part I. *IEEE Trans. Power Syst.* **2013**, *28*, 2554–2564. [CrossRef]
32. Bolognani, S.; Zampieri, S. On the Existence and Linear Approximation of the Power Flow Solution in Power Distribution Networks. *IEEE Trans. Power Syst.* **2016**, *31*, 163–172. [CrossRef]
33. Baran, M.E.; Wu, F.F. Network reconfiguration in distribution systems for loss reduction and load balancing. *IEEE Trans. Power Deliv.* **1989**, *4*, 1401–1407. [CrossRef]

Disclaimer/Publisher's Note: The statements, opinions and data contained in all publications are solely those of the individual author(s) and contributor(s) and not of MDPI and/or the editor(s). MDPI and/or the editor(s) disclaim responsibility for any injury to people or property resulting from any ideas, methods, instructions or products referred to in the content.